

# Deep Learning for Spatio-Temporal Fusion in Land Surface Temperature Estimation: A Comprehensive Survey, Experimental Analysis, and Future Trends

Sofiane Bouaziz<sup>\*†</sup>, Adel Hafiane<sup>\*</sup>, Raphaël Canals<sup>†</sup>, Rachid Nedjai<sup>‡</sup>

<sup>\*</sup> INSA CVL, PRISME UR 4229, Bourges, 18022, Centre Val de Loire, France

<sup>†</sup> Université d'Orléans, PRISME UR 4229, Orléans, 45067, Centre Val de Loire, France

<sup>‡</sup> Université d'Orléans, CEDETE, UR 1210, Orléans, 45067, Centre Val de Loire, France

**Abstract**—The rapid advancements in satellite remote sensing have enhanced the capability to monitor and analyze the Earth's surface. Among the many variables captured through satellite sensors, Land Surface Temperature (LST) plays a critical role in understanding key environmental processes. However, obtaining high-resolution LST data remains a challenge, as satellite sensors often face a trade-off between spatial and temporal resolutions. In response, Spatio-Temporal Fusion (STF) has emerged as a powerful method to integrate two satellite data sources, one providing high spatial but low temporal resolution, and the other offering high temporal but low spatial resolution. Although a range of STF techniques have been proposed, from traditional methods to cutting-edge deep learning (DL) models, most have focused on surface reflectance, with limited application to LST estimation. DL approaches, in particular, show promise in improving the spatial and temporal resolutions of LST by capturing complex, non-linear relationships between input and output LST data. This paper offers a comprehensive review of the latest advancements in DL-based STF techniques for LST estimation. We analyze key research developments, mathematically formulate the STF problem, and introduce a novel taxonomy for DL-based STF methods. Furthermore, we discuss the challenges faced by current methods and highlight future research directions. In addition, we present the first open-source benchmark STF dataset for LST estimation<sup>1</sup>, consisting of 51 pairs of MODIS-Landsat images spanning from 2013 to 2024. To support our findings, we conduct extensive experiments on state-of-the-art methods and present both quantitative and qualitative assessments. This is the first survey paper focused on DL-based STF for LST estimation. We hope it serves as a valuable reference for researchers and paves the way for future research in this field.

**Index Terms**—Spatio-temporal Fusion, Land Surface Temperature, Spatial Resolution, Temporal Resolution, Deep learning.

## I. INTRODUCTION

OVER the past decade, urbanization has intensified globally, with cities hosting an ever-increasing proportion of the world's population. As of 2020, more than half of the global population lives in urban areas, with European urbanization rates reaching 74% as early as 2017 [1]. However, this rapid expansion has amplified several environmental challenges, including the Urban Heat Island (UHI) effect, increased air and water pollution, and reduced green spaces. These issues collectively contribute to higher energy demands, deteriorating

air quality, and adverse public health impacts, such as respiratory illnesses and heat-related mortality, particularly in densely populated regions [2]–[4].

Land Surface Temperature (LST) emerged as an important variable for understanding and managing various environmental challenges. Physically, LST represents the thermal radiation emitted from the Earth's surface, influenced by how incoming solar energy interacts with the ground or the canopy in vegetated areas [5]. LST is regarded as a critical component of Earth system data by NASA and other international organizations [6], and is recognized by the Global Climate Observing System as one of the ten essential climate variables in the land biosphere [7]. It plays a key role in revealing the temporal and spatial dynamics of the surface's equilibrium state [8], [9]. This knowledge is fundamental for a wide array of applications, including climate monitoring [10], [11], urban planning [12], [13], and natural resource management [14], [15]. Satellites are the primary tool for collecting and measuring LST globally at a different scale averaged over space [16], which offers consistent LST data across large areas with frequent revisit times. As a result, many thermal infrared (TIR) sensors have been deployed on satellites, which lead to the development of various techniques for estimating LST at different spatial and temporal resolutions [17]–[23]. While satellite technology has made substantial advances in capturing precise LST observations, technical and budgetary constraints still impose a trade-off between spatial and temporal resolutions [24], [25]. *Spatial resolution* refers to the level of detail captured within a single pixel in an LST observation [26]. While *Temporal resolution* refers to the frequency of LST observations over time for a specific region [27]. However, simultaneously achieving both high spatial and high temporal resolution remains challenging, as higher spatial detail often necessitates a reduced frequency of re-visiting, while frequent observations generally rely on coarser spatial resolution [28].

Two main approaches have been identified in the literature for producing LST data with high spatial and temporal resolution [29]: *spatial downscaling* [28] and *Spatio-Temporal fusion* (STF) [30]. *Spatial downscaling*, also known as thermal sharpening or disaggregation, improves spatial resolution by assuming a consistent relationship between LST and auxiliary data at different scales [31]–[34]. For example, the thermal

<sup>1</sup>[https://github.com/Sofianebouaziz1/STF-LST\\_Dataset](https://github.com/Sofianebouaziz1/STF-LST_Dataset)

sharpening algorithm [31] uses auxiliary variables, such as normalized difference vegetation index (NDVI) and fractional vegetation cover, to estimate fine-scale LST values. This method has been expanded with additional inputs, including the normalized difference building index (NDBI) [35] and surface albedo [36]. However, downscaling is most effective over shorter time intervals, as the relationship between LST and auxiliary data from fine-resolution satellites may change over time [37].

*STF*, also known as data fusion or image fusion, is an alternative approach that combines two types of remote sensing (RS) data that share the same spectral information but differ in terms of resolution [38]. Typically, one data source offers high spatial but low temporal resolution (HSLT), while the other provides low spatial but high temporal resolution (LSHT) [39]. STF aims to integrate the data from these sources to produce LST observations that feature fine spatial and high temporal resolutions (HSHT) [38]. Figure 1 shows the trend in publications on STF for LST estimation between 2016 and 2024. The number of publications has grown significantly, with peaks in 2022 (417 papers) and 2024 (424 papers). This reflects the growing interest in HSHT LST research, motivated by not only advances in sensors but also by the urgent need to address increasing climate-related challenges. Despite a slight drop in 2023, the overall upward trend indicates an expansion of research and innovation in this field. STF techniques were initially developed for surface reflectance (SR) products but soon adapted for LST data [40]. STF techniques fall into four categories, as depicted in Figure 2: *weighted-based*, *unmixing-based*, *hybrid*, and *learning-based* methods.

*Weighted-based* methods predict fine-resolution images by incorporating neighborhood data [40]–[45]. One notable approach is the Spatial and Temporal Adaptive Reflectance Fusion Model (STARFM) algorithm [41], which adjusts the weights of adjacent pixels using separate conversion coefficients for homogeneous and heterogeneous regions. An improved version, Enhanced STARFM (ESTARFM) [42], further refines this algorithm by taking into account the variation between mixed and pure pixels, which leads to more precise weight adjustments. These methods are advantageous because they don't require extensive parameter learning from external data, making them fast and stable, especially in homogeneous areas. However, their reliance on homogeneity assumptions and low-pass filter-like models often leads to inadequate detail reconstruction. *Unmixing-based* methods treat temporal variations at coarse resolutions as mixtures of finer-scale variations [46]–[49]. An example is the spatial–temporal data fusion approach [46] which assumes that land cover types are stable over time, making it possible to transfer the SR variations of two adjacent high-resolution images obtained by unmixing to the low-resolution images. The Enhanced Spatial and Temporal Data Fusion Model [47] improves on this assumption by refining the classification, using sliding windows, and adding temporal weightings. These methods capture some details but emphasize spatial and spectral relationships rather than temporal ones, often resulting in blocky artifacts. *Hybrid* methods integrate elements from both *weighted-based*

and *unmixing-based* approaches to leverage their respective strengths [50]–[53]. For instance, the method proposed in [53] uses a kernel-driven fusion approach that combines spatial weighting and unmixing principles to produce downscaled LST observations. However, its accuracy diminishes as the time interval between kernels increases.

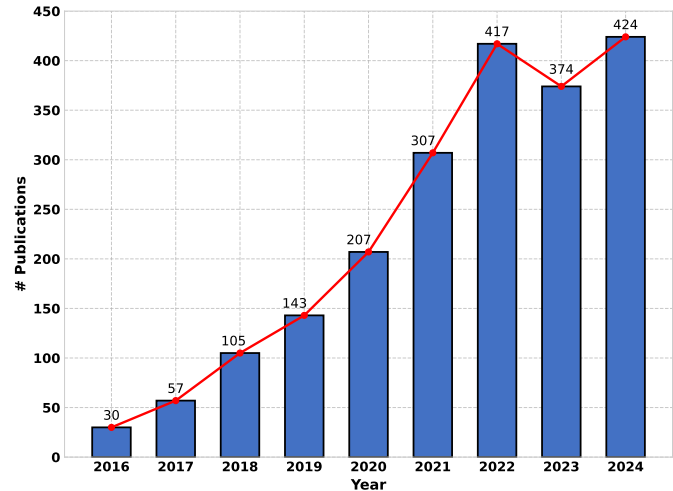


Fig. 1. Yearly literature count related to STF for LST estimation indexed by Google Scholar since 2016. The search query also covered the synonyms of Spatio-Temporal Fusion, such as data fusion and image fusion.

*Learning-based* methods are data-driven approaches that rely on training models with existing datasets to establish relationships between HSLT and LSHT images. These methods are classified into two main categories: *sparse representation-based* (or dictionary learning) and *deep learning-based* (DL) algorithms. Sparse representation-based methods, considered as shallow learning techniques [54]–[57], leverage techniques like Bayesian learning to model coarse-to-fine images. Bayesian approaches use temporal correlations within image time series to recast fusion as an estimation problem, aiming to maximize posterior probabilities. Examples include covariance functions [58], low-pass filtering [59], pixel unmixing [60], joint Gaussian distribution [61], and Kalman filters [62]. The primary limitations of this method are its strong dependence on the image range and the inherent complexity of the model [63]. DL-based methods have the advantage of establishing non-linear relationships between input and output images, which set them apart from other approaches. Various architectures have been explored, including Convolutional Neural Networks (CNNs) [39], [64]–[72], AutoEncoders (AEs) [63], [73], [74], Generative Adversarial Networks (GANs) [75]–[83], Vision Transformers [74], [84]–[88], and Recurrent Neural Networks (RNN) [72], [89], [90]. However, unique challenges in STF remain and require further investigation. This survey aims to guide future advances in this field.

A variety of surveys have been proposed for STF of satellite imagery in RS. Table I provides a comparison between existing STF surveys and our own, using seven key criteria. The first criterion is the *year* of publication. We prioritize surveys with more recent dates as they cover the latest advancements in

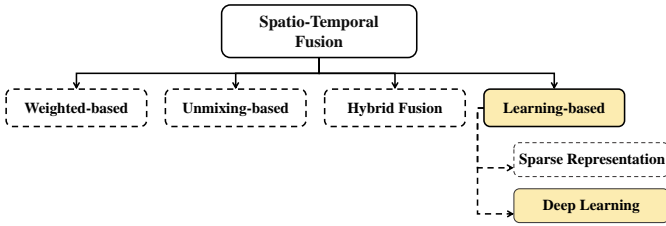


Fig. 2. Taxonomy of STF methods. This survey focuses on DL-based STF approaches for LST estimation.

STF methods, which, as shown in Figure 1, are continuously evolving. Next is the *scope*, which could be either SR, LST, or NDVI. For LST-focused surveys, we check whether they discuss how to *adapt* the SR STF methods for LST STF specifically. Another criterion is the inclusion of *DL*. It's important to note that merely mentioning DL methods is not sufficient. A survey should at least outline the neural network (NN) architectures used and explain their objectives and implementation details. If DL methods are covered, we then assess whether the survey describes the *limitations* of these techniques and identifies open research areas. We also evaluate whether the surveys *conducted experiments* to validate STF methods, and whether they *proposed a new dataset* to support their findings. To the best of our knowledge, only three surveys [91]–[93] have addressed STF for LST estimation. However, none have thoroughly explored the potential of learning-based approaches, especially DL techniques, for this problem. Moreover, no experimental studies were conducted, and instead, they assume that fusion methods designed for SR can be seamlessly applied to LST.

In this survey, we provide a comprehensive review of DL-based methods for LST estimation. We propose a new mathematical definition for the multi-objective problem and introduce a novel taxonomy based on four criteria to classify existing methods. Additionally, we present a new MODIS-Landsat LST pair dataset, consisting of 51 images, which, to the best of our knowledge, is the first, largest, and most recent open-source dataset available in this field. Through extensive experimental analysis, we evaluate different state-of-the-art methods using both quantitative and qualitative assessments, which offers insights into the application of STF for LST estimation. We also highlight the limitations of current approaches and suggest potential avenues for future research.

Our review is organized into several sections. In Section II, we provide an in-depth examination of satellite-derived LST, beginning with an overview of the LST concept and its retrieval from satellite imagery. We further explore the trade-offs between spatial and temporal resolution, emphasizing how these factors influence the accuracy of LST estimates. Section III formally defines the STF problem for LST estimation. We introduce a mathematical formulation of STF, discuss the different loss functions employed in STF methods, and detail the evaluation metrics used to assess the performance of these approaches. In Section IV, we propose a novel taxonomy for DL-based STF methods. Section V presents our

experimental study. We introduce the new dataset used for this research comprising paired MODIS and Landsat LST data and evaluate the performance of various DL-based STF methods. In Section VI, we examine the limitations of current DL-based STF methods for LST estimation and discuss promising future trends, highlighting unresolved challenges and open research questions. Finally, Section VII concludes the review by summarizing our findings.

## II. SATELLITE-DERIVED LST

In this section, we will define LST, explain how it is derived from satellite observations, and discuss the challenges associated with the trade-off between spatial and temporal resolution in satellite data.

### A. LST Concept and Retrieval

LST is defined as the thermodynamic temperature at the surface of objects. In RS, this surface layer is continuous and projected across all visible components within the sensor's instantaneous field of view (IFOV), as shown in Figure 4. RS LST is called radiometric temperature [103], as it requires eliminating atmospheric effects and correcting for emissivity. Its formula is described in the equation 1 [16], [104], [105].

$$T_s(\theta_v, \varphi_v) = B_\lambda^{-1} \left[ \frac{A}{B} \right] \quad (1)$$

$$A = R_\lambda(\theta_v, \varphi_v) - R_{at\lambda\uparrow}(\theta_v, \varphi_v) - \tau_\lambda(\theta_v, \varphi_v) [1 - \varepsilon_\lambda(\theta_v, \varphi_v)] R_{at\lambda\downarrow}$$

$$B = \tau_\lambda(\theta_v, \varphi_v) \varepsilon_\lambda(\theta_v, \varphi_v)$$

where  $T_s$  is the radiometric temperature,  $\theta_v$  and  $\varphi_v$  represent the viewing zenith and azimuth angles,  $\lambda$  is the channel-effective wavelength.  $B_\lambda^{-1}$  is the inverse function of Planck's law, which converts the measured radiance into temperature.  $R_\lambda$ ,  $R_{at\lambda\uparrow}$ , and  $R_{at\lambda\downarrow}$  are the at-sensor observed radiance, upward atmospheric radiance, and downward atmospheric radiance respectively,  $\tau_\lambda$  is the channel atmospheric transmittance, and  $\varepsilon_\lambda$  is the channel land surface emissivity (LSE).

The radiometric temperature has four properties:

- 1) It is independent of spatial scale, meaning it can be applied across various scales [107].
- 2) The depth of penetration depends on the wavelength used. In TIR range ( $\lambda \approx 10 \mu\text{m}$ ), the depth varies from 1 to 100  $\mu\text{m}$ , leading to the term skin temperature [103]. In the microwave range ( $\lambda \approx 1 \text{cm}$ ), the depth ranges from 0.1 to 10 cm, hence the term subsurface temperature [108].
- 3) It is affected by the viewing angle, making it directional [103].
- 4) It represents an average temperature derived from all homogeneous and isothermal elements within the IFOV [103]

Retrieving LST from these radiances presents a challenging and ill-posed problem due to the following reasons:

TABLE I  
COMPARISON OF EXISTING STF SURVEYS FOR SATELLITE IMAGERY IN RS AND OUR SURVEY.

Survey	Year	Scope	Adaptation	Deep learning	Limitations	Conducted Experiments	Proposed New Dataset
[38]	2018	SR	✗	✗	✗	✗	✗
[30]	2019	SR	✗	✗	✗	✗	✗
[94]	2020	SR	✗	✓	✗	✓	✓
[92]	2020	LST	✗	✗	✗	✗	✗
[68]	2020	SR	✗	✓	✓	✓	✗
[91]	2021	LST	✗	✗	✗	✗	✗
[95]	2022	NDVI	✗	✓	✓	✗	✗
[96]	2023	SR	✓	✗	✓	✓	✗
[97]	2023	SR	✗	✗	✗	✗	✗
[98]	2023	SR	✗	✓	✓	✗	✗
[99]	2023	SR	✗	✗	✗	✗	✗
[100]	2024	SR	✗	✗	✗	✗	✗
[101]	2024	SR	✗	✗	✗	✗	✗
[93]	2024	LST	✓	✗	✗	✗	✗
[102]	2024	SR	✗	✗	✗	✗	✗
Our survey	2024	LST	✓	✓	✓	✓	✓

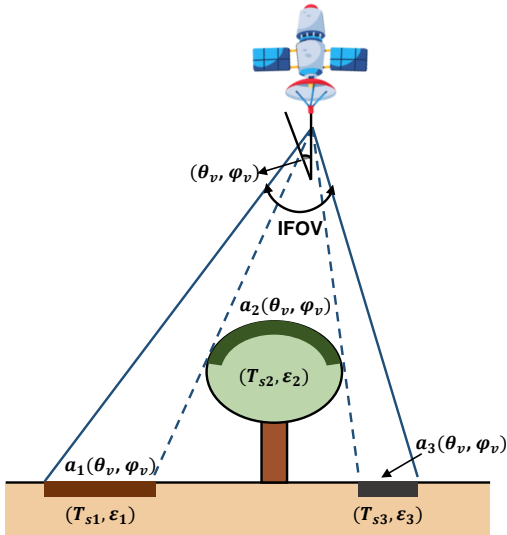


Fig. 3. Schematic representation of the Satellite-derived LST, inspired by [106].  $T_{s_i}$ ,  $\varepsilon_i$ , and  $a_i$  represent the surface temperature, emissivity, and projected area weight for the  $i$ -th visible component, respectively.  $\theta_v$  is the view zenith angle, and  $\varphi_v$  is the viewing azimuth angle.

- LST retrieval is underdetermined because, for every radiance measurement across  $N$  TIR channels, there are  $N$  unknown LSEs and an unknown LST.
- The radiances measured in different TIR channels are highly correlated, making the system of equations unstable and sensitive to small errors in the data.

To overcome these challenges, additional assumptions and constraints are required to either increase the number of equations or reduce the number of unknowns, while also decor-

relating the data. Consequently, several algorithms have been developed to retrieve LST, including the Single-Channel [109], Split-Window [110], mono-window [111], and others.

### B. Trade-offs in Spatial and Temporal Resolution for LST Retrieval

The accuracy of LST retrieval is significantly influenced by two key factors: *spatial resolution* and *temporal resolution*.

- **Spatial Resolution:** defines the size of a pixel in the satellite image, which determines the smallest detectable feature. This is crucial for accurate LST retrieval, as fine-scale spatial resolution captures smaller, more localized temperature variations [27].
- **Temporal Resolution:** refers to the frequency at which a satellite revisits the same area. A higher temporal is critical for monitoring dynamic temperature changes over time [28].

Table II presents the most common satellites for retrieving LST. It highlights the inherent trade-off between spatial and temporal resolution. For example, satellites like Landsat 8 and Landsat 9 offer a good spatial resolution of 30 m, but their temporal resolution is limited to 16 days. On the other hand, satellites like MODIS Aqua and MODIS Terra provide a much higher temporal resolution 1 day, but with a coarser spatial resolution 1 km. To address this, STF techniques offer a promising solution and will be discussed in the next sections.

### III. STF PROBLEM FORMULATION

This section defines the STF problem mathematically, introduces the relevant notations, and explains how DL is integrated. It also categorizes the various loss functions used

TABLE II  
COMPARISON OF COMMON SATELLITE-BASED LST PRODUCTS WITH THEIR THERMAL SENSORS, SPATIAL AND TEMPORAL RESOLUTIONS, AND TEMPORAL EXTENTS.

Satellite	Thermal Sensor	Spatial Resolution	Temporal Resolution	Temporal Extent
GF-5	VIMS	40 m	7 days	2018/05/09 - Present
Landsat 9	TIRS-2	100 m, resampled to 30 m	16 days	2021/09/27 - Present
Landsat 8	TIRS	100 m, resampled to 30 m	16 days	2013/02/11 - Present
Landsat 7	ETM+	100 m, resampled to 30 m	16 days	1999/04/15 - Present (Partially)
Landsat 5	TM	120 m, resampled to 30 m	16 days	1984/05/01 - 2013/06/05
Terra	Aster	90 m	16 days	18/12/18 - Present
Aqua	MODIS	1 km	1 day	2002/05/04 - Present
Terra	MODIS	1 km	1 day	199/12/18 - Present
Sentinel-3A	SLSTR	1 km	1 day	2016/02/16 - Present
FY-3D	MERSI-2	375 m	12 hours	2017/11/15 - Present
SNPP	VIIRS	375 m	12 hours	2011/11/28 - Present
GOES-8	IMAGER	4 km	30 minutes	1994/09/16 - 2009/06/04
FY-2F	VISSR	5 km	1 hour	2012/01/13 - Present

during the training process and presents the evaluation metrics employed to assess model performance.

#### A. Mathematical Definition of STF

The STF problem can be viewed as a multi-objective optimization problem, wherein the goal is to simultaneously enhance both the spatial and temporal resolution, as shown in equation 2.

$$\max(\mathcal{F}(R_s), \mathcal{F}(R_t)) \quad (2)$$

where,  $\mathcal{F}(R_s)$  and  $\mathcal{F}(R_t)$  represent the objectives corresponding to spatial and temporal resolution enhancement, respectively. However, an additional, often overlooked, objective is the gap filling in the high-resolution image. This makes the STF problem a tri-objective optimization problem that aims to balance spatial and temporal resolution enhancement along with the efficient filling of gaps.

STF methods are primarily based on the use of known characteristics of image pixel values over time, called *temporal variations*, and at different spatial scales, called *spatial variations*, to estimate HSHT satellite images. For LST, *temporal variations* refer to changes in the values observed in the same area over time, while differences in *spatial variations* refer to changes in the number and type of pixels between LSHT and HSLT images.

Let  $X_1$  and  $X_2$  represent the data from two satellites: the first,  $X_1$ , provides LST data with LSHT, and the second,  $X_2$ , provides LST data with HSLT. Let  $t_1, t_2, t_3$  be three distinct time steps, and let  $s$  denote the region of interest. Therefore,  $X_1(s, t_i)$  and  $X_2(s, t_i)$  for  $i \in \{1, 2, 3\}$  represent the LST data from the first or second satellite at time  $t_i$  at location  $s$ . Given two pairs of satellite images,  $P_1 = \{X_1(s, t_1), X_2(s, t_1)\}$  and  $P_3 = \{X_1(s, t_3), X_2(s, t_3)\}$ , at times  $t_1$  and  $t_3$ , along with the

image  $X_1(s, t_2)$  at time  $t_2$ , the objective of STF is to predict  $X_2(s, t_2)$ , as illustrated on Figure 4. The various notations used in this formulation are summarized in Table III.

TABLE III  
NOTATIONS USED IN STF-PROBLEM FORMULATION.

Notation	Significance
$X_1$	Satellite providing LST data with LSHT
$X_2$	Satellite providing LST data with HSLT
$t_i$	Temporal time steps
$s$	Region of interest
$X_i(s, t_i)$	LST data at time $t_i$ for the region $s$
$\hat{X}_2(s, t_i)$	Predicted high spatial LST data at time $t_i$ and for region $s$
$P_i$	A pair of $X_1$ and $X_2$ for a specific region $s$ at time $t_i$

Given the previous description, the predicted high spatial resolution image at time  $t_2$ , denoted as  $\hat{X}_2(s, t_2)$ , can be defined as in equation 3. The goal is for  $\hat{X}_2(s, t_2)$  to be as close as possible to the real  $X_2(s, t_2)$ .

$$\hat{X}_2(s, t_2) = f(P_1, P_3, X_1(s, t_2)). \quad (3)$$

However, this problem cannot be adequately solved using linear methods [48], [112], [113]. As a result, non-linear approaches, such as DL, are more suitable. DL is a subset of machine learning that employs neural networks with multiple layers to learn complex and non-linear relationships in data. To account for these non-linear dependencies, the function  $f$  is modified to include weights  $\mathbf{W}$  that are optimized during training, as shown in equation 4.

$$\hat{X}_2(s, t_2) = f(P_1, P_3, X_1(s, t_2) | \mathbf{W}). \quad (4)$$

In certain cases, relying on two pairs of images may not be optimal, as it requires waiting for a future pair,  $P_3$ , captured

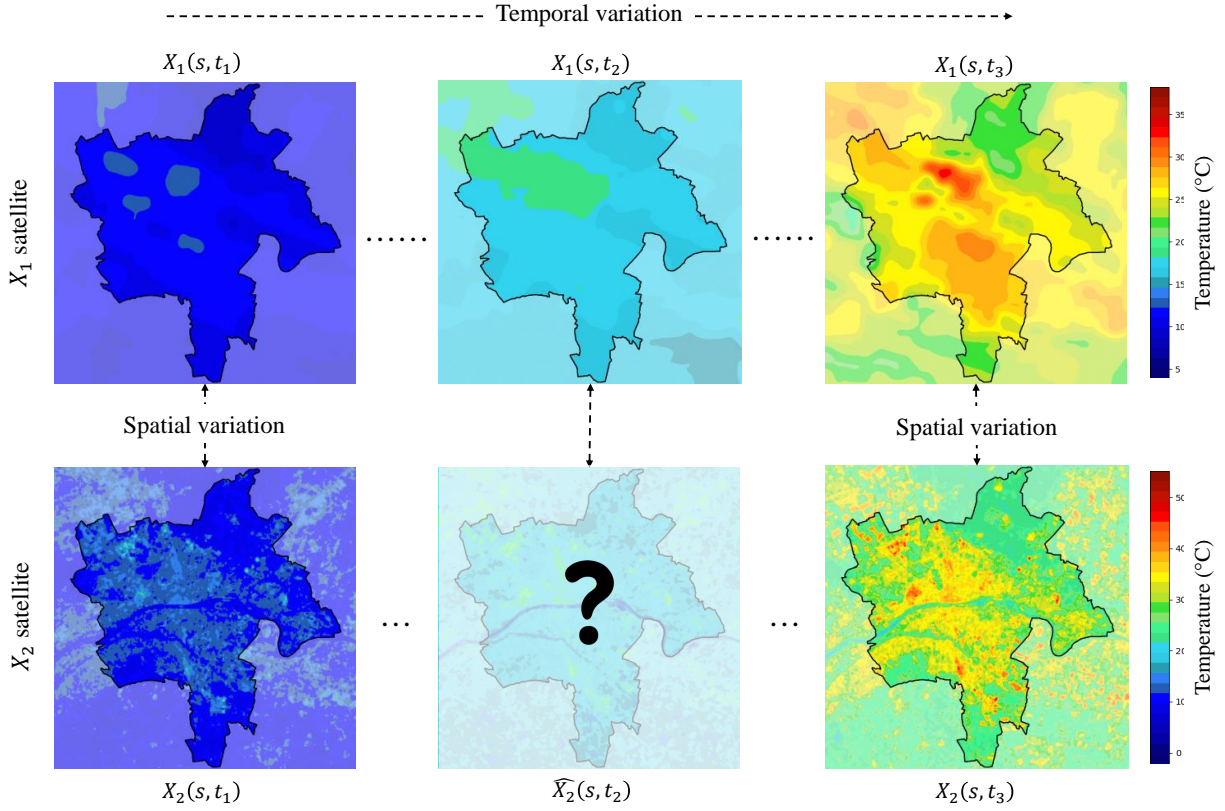


Fig. 4. Graphic representation of the STF for LST process. In this example,  $X_1$  denotes data from the MODIS Terra satellite, and  $X_2$  refers to data from the Landsat 8 satellite. The region of interest,  $s$ , corresponds to Orléans Métropole in the Centre-Val de Loire region, France. The time steps  $t_1$ ,  $t_2$ , and  $t_3$  represent March 6, March 22, and May 9, 2022, respectively.

under favorable climate conditions (e.g., minimal cloud coverage) to accurately predict the high spatial resolution data at an earlier time. To overcome this limitation, two alternative strategies have been proposed. The first approach involves using only one pair of images, which we denote as  $P_1$ . The second approach leverages a time series of previous pairs, which can be particularly advantageous for models like RNNs, such as LSTM, that can exploit temporal dependencies for better prediction.

### B. Loss functions

The weights  $\mathbf{W}$  introduced in Equation 4 are learned using a loss function that measures the difference between  $\hat{X}_2(s, t_2)$  and  $X_2(s, t_2)$  in different levels and is denoted as  $\text{Loss}(\hat{X}_2, X_2)$ . Common forms of the loss function are presented in this subsection.

1) *Content Loss*: It ensures that the reconstructed image preserves the overall texture and tone of the ground truth image. It includes metrics such as the Mean Squared Error (MSE), which quantifies the average squared difference between the pixel intensities of the predicted and reference images, as shown in Equation 5. Another example is the Mean Absolute Error (MAE), Euclidean distance [114], Frobenius norm [115], Kullback–Leibler (KL) Divergence [116], and the Huber loss [117]. Additionally, some works incorpo-

rate satellite-derived indices, such as the NDVI [118] and NDBI [119], into the loss function to guide the fusion process.

$$\mathcal{L}_{\text{content}} = \frac{1}{N} \sum_{i=1}^N \left( \hat{X}_2(s_i, t_2) - X_2(s_i, t_2) \right)^2 \quad (5)$$

2) *Vision loss*: It quantifies the overall quality of the image, particularly from a human visual perception standpoint. A common measure used to assess it is the Structural Similarity Index (SSIM) [120], which evaluates the similarity of images by considering three aspects: luminance, contrast, and structure, as formulated in Equation 6. Another example is the multi-scale SSIM (MS-SSIM) [121].

$$\mathcal{L}_{\text{vision}} = \frac{(2\mu_{\hat{X}_2(s, t_2)}\mu_{X_2(s, t_2)} + C_1)(2\sigma_{\hat{X}_2 X_2(s, t_2)} + C_2)}{(\mu_{\hat{X}_2(s, t_2)}^2 + \mu_{X_2(s, t_2)}^2 + C_1)(\sigma_{\hat{X}_2(s, t_2)}^2 + \sigma_{X_2(s, t_2)}^2 + C_2)} \quad (6)$$

where  $\mu_{\hat{X}_2(s, t_2)}$  and  $\mu_{X_2(s, t_2)}$  are the means of the predicted and ground truth images,  $\sigma_{\hat{X}_2(s, t_2)}$  and  $\sigma_{X_2(s, t_2)}$  are their variances, and  $\sigma_{\hat{X}_2 X_2(s, t_2)}$  is the covariance between the predicted image  $\hat{X}_2(s, t_2)$  and the ground truth image  $X_2(s, t_2)$ . Constants  $C_1$  and  $C_2$  are used to stabilize the division.

Additionally, Sobel loss calculates the MSE loss of features after passing through the Sobel operator [122]. This loss

effectively captures the degree of texture detail restoration in images and is formulated in Equation 7.

$$\mathcal{L}_{\text{vision}} = \frac{1}{N} \sum_{i=1}^N \left[ f_{\text{sobel}}(\hat{X}_2(s, t_2)) - f_{\text{sobel}}(X_2(s, t_2)) \right]^2 \quad (7)$$

where  $f_{\text{sobel}}(\hat{X}_2(s, t_2))$  and  $f_{\text{sobel}}(X_2(s, t_2))$  represent the feature maps of the predicted and ground truth images after applying the Sobel operator, respectively.

3) *Feature Loss*: It captures high-level perceptual features by comparing intermediate representations obtained from pre-trained networks [123], such as autoencoders. Typically, only the encoder part of these networks is used to extract the features. The feature loss can then be formulated as the difference between the features of the predicted image  $\tilde{F}_{\hat{X}_2}$  and the target image  $F_{X_2}$ , obtained from the encoder, as expressed in equation 8. Where  $L$  is the total number of features per image.

$$\mathcal{L}_{\text{feature}} = \frac{1}{L} \|F_{\tilde{X}_2} - F_{X_2}\|_2^2 \quad (8)$$

4) *Spectral loss*: It measures the cosine similarity between the predicted and ground truth images in the feature space, typically obtained from a pre-trained model [77]. Unlike feature loss, spectral loss focuses on the spectral characteristics of the images, ensuring that the predicted image maintains similar feature distributions and spectral content as the ground truth, as defined in equation 9.

$$\mathcal{L}_{\text{Spectral}} = 1 - \frac{F_{\tilde{X}_2} \cdot F_{X_2}}{\|F_{\tilde{X}_2}\| \|F_{X_2}\|} \quad (9)$$

5) *Adversarial Loss*: Denoted as  $L_{\text{GAN}}$  and is used in generative models. It ensures that the generated images are indistinguishable from real images [124]. This loss will be detailed in section IV-A3.

Therefore, the total loss function can be formulated as a weighted sum of the individual loss components described above, as shown in Equation 10.

$$\mathcal{L}_{\text{total}} = \lambda_1 \mathcal{L}_{\text{content}} + \lambda_2 \mathcal{L}_{\text{vision}} + \lambda_3 \mathcal{L}_{\text{feature}} + \lambda_4 \mathcal{L}_{\text{Spectral}} + \lambda_5 \mathcal{L}_{\text{GAN}} \quad \text{where} \quad \sum_{i=1}^5 \lambda_i = 1 \quad (10)$$

Furthermore, these loss functions are optimized using various algorithms, including the Stochastic Gradient Descent and Adam Optimizer [125].

### C. Evaluation Metrics

Similar to computer vision (CV) tasks, STF models utilize a range of evaluation metrics that can be categorized into three key groups: *Error Assessment Metrics*, *Quality Assessment Metrics*, and *Computational Assessment Metrics*

1) *Error Assessment Metrics*: These metrics quantify the numerical discrepancy between the fused image and the reference image, which provides a quantitative measure of accuracy. Key examples include the *Root MSE (RMSE)*, which is derived from Equation 5, as well as the MAE, relative MAE (rMAE), Mean Absolute Errors Change (MAEC) and the Coefficient of Determination ( $R^2$ ). Additionally, the *Error Relative Global Dimensionless Synthesis (ERGAS)* assesses the normalized error between  $\hat{X}_2(s, t_i)$  and  $X_2(s, t_i)$ , as described in Equation 11. Lower ERGAS values indicate greater fidelity to the reference image.

$$\text{ERGAS} = 100 \cdot \frac{h}{l} \sqrt{\frac{1}{N} \sum_{k=1}^N \left( \frac{\text{RMSE}(B_k)}{\mu_k} \right)^2} \quad (11)$$

where  $h$  and  $l$  are the spatial resolutions of the high- and low-resolution images,  $N$  is the number of bands (here  $N = 1$ ),  $\text{RMSE}(B_k)$  is the root mean square error for band  $k$ , and  $\mu_k$  is the mean value of band  $k$  in  $X_2(s, t_i)$ .

2) *Quality Assessment Metrics*: These metrics assess the structural or perceptual similarity between the fused image and the reference image. The *SIIM* quantifies perceptual similarity, ranging from 0 (no similarity) to 1 (perfect similarity) [120], as defined in Equation 6. The *Peak Signal-to-Noise Ratio (PSNR)* measures the quality of  $\hat{X}_2(s, t_i)$  relative to  $X_2(s, t_i)$  by comparing the maximum pixel value of the reference image to the level of distortion [126]. Higher PSNR values indicate better quality. It is calculated as in Equation 12.

$$\text{PSNR} = 10 \cdot \log_{10} \left( \frac{P_{\text{max}}^2}{\text{MSE}} \right) \quad (12)$$

where  $P_{\text{max}}$  represents the maximum pixel value of the reference image. The *Correlation Coefficient (CC)* measures the linear relationship between  $\hat{X}_2(s, t_i)$  and  $X_2(s, t_i)$ , with values ranging from -1 to 1, where values closer to 1 indicate a strong positive correlation [127]. The CC is computed as in Equation 13.

$$\text{CC} = \frac{\sum (\hat{X}_2(s, t_i) - \tilde{\bar{X}})(X_2(s, t_i) - \bar{X})}{\sqrt{\sum (\hat{X}_2(s, t_i) - \tilde{\bar{X}})^2 \sum (X_2(s, t_i) - \bar{X})^2}} \quad (13)$$

where  $\tilde{\bar{X}}$  and  $\bar{X}$  are the mean values of  $\hat{X}_2(s, t_i)$  and  $X_2(s, t_i)$ , respectively. The *Spectral Angle Mapper (SAM)* calculates the angle between two image vectors  $\hat{X}_2(s, t_i)$  and  $X_2(s, t_i)$ , with smaller angles indicating greater similarity [128]. SAM ranges from  $0^\circ$  (perfect similarity) to  $90^\circ$  (orthogonality, or complete dissimilarity). SAM is defined as in Equation 14.

$$\text{SAM} = \arccos \left( \frac{\mathbf{a} \cdot \mathbf{b}}{\|\mathbf{a}\| \|\mathbf{b}\|} \right) \quad (14)$$

where  $\mathbf{a}$  and  $\mathbf{b}$  are the pixel vectors for the predicted and reference images, respectively. Other quality assessment metrics, such as the Universal Image Quality Index (UIQI) [129], Perceptual Image Patch Similarity (LPIPS) [130], and Q4 [131], can also be used.

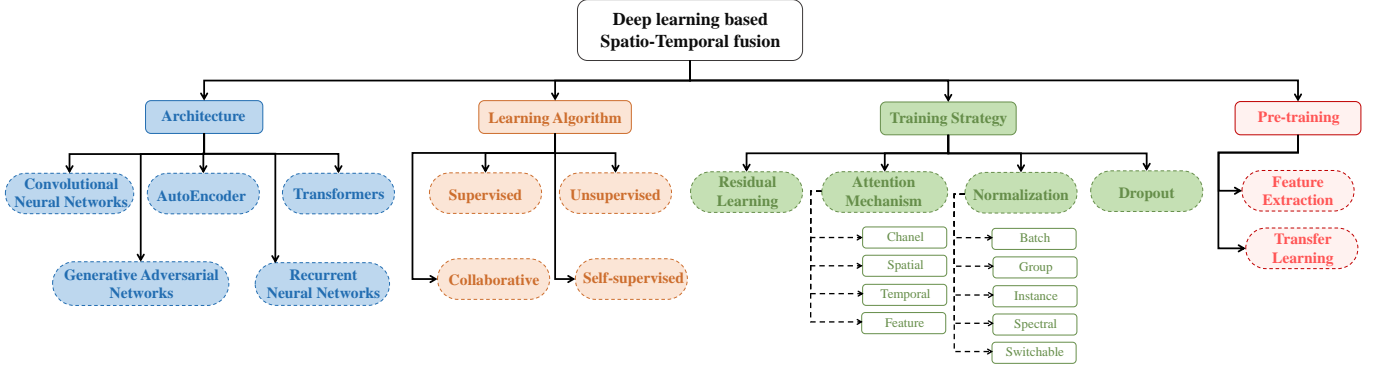


Fig. 5. Proposed Taxonomy for DL-Based STF Methods: Classification Based on Architecture, Learning Algorithm, Training Strategy, and Incorporation of Pre-trained Models.

3) *Computational Assessment Metrics*: Computational efficiency, while often overlooked, is a crucial aspect of evaluating the performance of STF models. The time cost for generating fused images plays a vital role in real-time applications requiring quick processing. Once the model is trained, the time taken to fuse a single test image is measured to assess the model's efficiency. This metric becomes even more critical in real-world challenges, where the ability to process and generate fused images rapidly can significantly impact decision-making and operational workflows. For instance, the DL-based method proposed by [76] took only 0.29 seconds to generate a fused image, while the traditional ESTARFM algorithm required 85.71 seconds for the same task.

#### IV. TAXONOMY OF DL-BASED STF METHODS

In this section, we propose a new taxonomy to classify Deep Learning (DL)-based Spatio-Temporal Fusion (STF) methods. We constructed this taxonomy, we selected 30 methods based on recency, consistency, and relevance. The classification is organized around four key criteria, as illustrated in Figure 5: *Architecture*, *Learning Algorithm*, *Training Strategy*, and *Incorporation of Pre-trained Models*. For each criterion, we categorize the methods into corresponding sub-criteria, ensuring a structured analysis that captures the diversity and unique characteristics of each approach.

##### A. Architectures

The primary criterion for differentiating DL-based STF methods is the underlying model architecture, which can be based on *CNNs*, *AEs*, *GANs*, *Vision transformers*, or *RNNs*.

1) *Convolutional Neural Networks*: CNNs are among the most well-known and widely used architectures designed to efficiently process grid-like data structures such as images [132]–[134]. CNNs are a feed-forward neural network that has significantly advanced the field of image analysis and CV [135]. One of the key advantages of CNNs over traditional neural networks is their ability to automatically identify and learn relevant features from input data without requiring human supervision [136]. This makes CNNs highly effective at extracting complex spatial hierarchies from images, such

as edges, textures, and shapes. A CNN consists of a series of layers between the input and output, typically including: *convolutional*, *pooling*, *normalization*, *activation*, and *fully connected* layers [137].

- *Convolutional Layers*: Perform convolution operations using multiple local filters to extract spatial features from the input data, which produce feature maps that capture important patterns.
- *Pooling Layers*: Reduce the spatial dimensions of feature maps, which helps to decrease computational load and makes the learned features more robust to variations and distortions in the input.
- *Normalization Layers*: Improve the stability and convergence of the network during training.
- *Activation Layers*: Apply non-linear functions, like Rectified Linear Unit (ReLU) [138], to increase the network's ability to model complex relationships within data.
- *Fully Connected Layers*: Integrate the features learned from previous layers and use them to make final predictions or classifications.

CNNs have evolved considerably since their introduction in the 1980s [139]. [140] introduced LeNet-5 in 1998, a CNN model designed to classify handwritten digits from the MNIST dataset, based on convolutional and fully connected layers. In 2012, AlexNet [132] revolutionized CNNs by achieving state-of-the-art results on the ImageNet dataset [141] through deeper architecture, smaller filters, and an increased number of hidden units. VGG [142] maintained strong performance with a simpler design, while GoogLeNet [143] used Inception modules for multi-scale feature learning. In 2016, ResNet [144] introduced residual connections for very deep networks, also excelling on ImageNet. Later models like DenseNet [145], ResNeXt [146] and EfficientNet [147] enhanced feature reuse and scaling efficiency.

CNN-based STF methods leverage CNN to automatically capture and model the complex, non-linear relationships between LSHT and HSLT image pairs. These learned relationships are then used to predict target images at a fine spatial resolution. Although CNNs are primarily designed for spatial modeling, they can be adapted to incorporate temporal information. This is achieved by processing multiple temporal images through



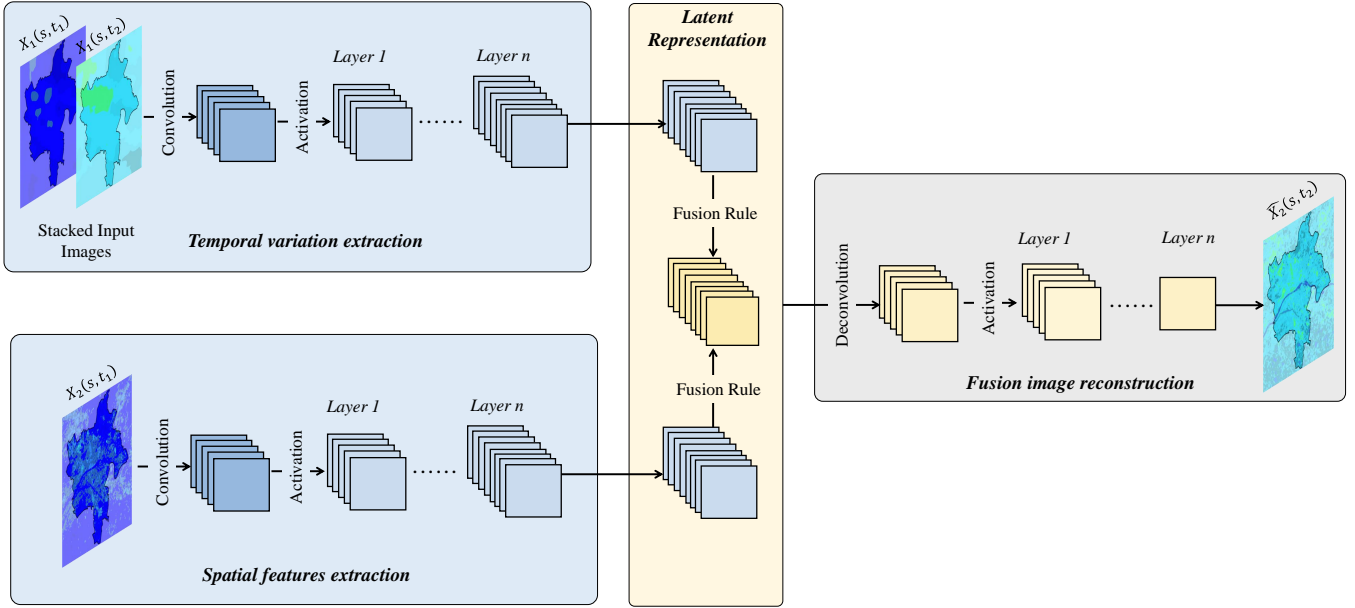


Fig. 6. Typical architecture of a CNN-based STF method using a single pair of images,  $P_1$ , composed of four main blocks: spatial feature extraction, temporal variation extraction, fusion of spatial and temporal representations, and image reconstruction. The fusion rule can be Element-wise Addition, Multiplication, Concatenation, Attention, etc.

separate CNNs and then combining the outputs to account for both spatial and temporal variations. Figure 6 illustrates the typical architecture of a CNN-based STF method, using a single  $P_1$  pair of images. The network is structured into four main blocks. First, the spatial feature extraction block processes the high-resolution image through several convolutional layers to derive a compressed feature representation. The second block, dedicated to temporal variation extraction, concatenates two low-resolution images along separate channels. These are then passed through convolutional layers to capture and compress temporal features. The spatial and temporal representations are subsequently fused in a latent space. Following this, a deconvolutional process and a series of fully connected layers are employed to reconstruct the predicted high-resolution image. When additional image pairs are used, a similar architecture is applied, with weighted results from each pair integrated to produce the final prediction.

In [39], the first STF method using CNNs was proposed for MODIS and Landsat images to generate HSHT with 30m spatial resolution and 1-day temporal resolution. The approach involves training the CNN on  $n$  MODIS and Landsat pairs to learn the non-relationship between them. During the prediction phase, only  $P_1$  and  $P_3$  are used to predict the desired image for the given date. They employed a content-based loss function, specifically the MSE. The method was tested on the CIA and LGC datasets [148]. A comparable approach was developed by [66]. [68] extended this approach by using two prior pairs instead of one and applying the Euclidean distance as the loss function. [64] proposed a reformulation of the problem that aligns with the previous definition provided in Section III-A. In their method, only one pair of images,  $P_1$ , and  $X_1(s, t_2)$  is used to predict  $X_2(s, t_2)$ . The architecture is composed of two main blocks: the first block captures the spatial information of

the Landsat image at time  $t_1$ , while the second block models the temporal variation between  $X_1(s, t_1)$  and  $X_1(s, t_2)$ . These blocks are processed through multiple convolution layers, which are then fused at an intermediate stage. Following this, deconvolution and fully connected layers are applied to generate the output image  $\hat{X}(s, t_2)$ . The MSE served as the optimization loss function. The data in this study was manually collected and corrected by the authors. [69] introduced a sensor bias-driven STF model, which addresses the spectral and spatial distortions between different sensors by explicitly modeling sensor bias. The method uses a dual CNN approach. One CNN enhances coarse reflectance images, while another learns the bias between Landsat and MODIS sensors. [70] proposed a multi-constrained loss function. This loss function not only improves the quality of the fusion results but also addresses the problem of gap-filling by utilizing cloud-contaminated images. A distinctive feature of this approach is that the fusion model automatically learns how to handle gaps in the data. The predicted image pixels are multiplied by a mask, which takes a value of 0 for empty (cloud-contaminated) pixels and 1 for valid (non-empty) pixels. [149] introduce an unsupervised learning approach based on CNNs to fuse Landsat-8 and Sentinel-2 data. Unlike previous methods, [72] proposes a hybrid approach that integrates a multiscale Siamese CNN to extract spatial-spectral features and a multilayer convolutional RNN with convolutional LSTM units to model the temporal and spectral dynamics of land cover changes. However, these previous methods were tested on SR data, with no validation conducted for LST data. [67] proposed an STF method for LST estimation called STTFN which uses two independent CNNs : forwardCNN and backwardCNN. The forwardCNN takes a pair  $P_1$  and  $X_1(s, t_3)$  to predict  $X_2(s, t_3)$ , while the backwardCNN uses  $P_3$  and  $X_1(s, t_1)$  to predict  $X_2(s, t_1)$ .

During training, the two models are trained separately. At the evaluation stage, the forwardCNN is applied with  $P_2$  and  $X_1(s, t_1)$ , and the backwardCNN with  $P_2$  and  $X_1(s, t_3)$ . The final fused estimate  $X_2(s, t_2)$  is obtained by applying a weighting function to combine the predictions from both models. This approach was tested on LST data and utilized the Huber loss as the content loss to mitigate the influence of abnormal values in the input LST images. The authors applied spatial interpolation (bicubic) to resize the MODIS images to match the size of Landsat images. [71] proposed a cascade STF method that utilizes multiple temporal pairs to predict LST at a given time  $t_1$ . Instead of just using a prior and subsequent pair, the framework takes  $n$  pairs, starting from time  $t_0$  (the prior) and then from  $t_2$  to  $t_n$  (subsequent times). The first block of the architecture is a supervised model that extracts spatial features to generate initial fusion results from auxiliary data. Then, a self-supervised model refines these results by leveraging spatiotemporal features at the prediction dates. In addition to the previously mentioned loss functions, two other loss functions are introduced specifically for the use of  $n$  temporal pairs: cycle consistency loss, which constrains the relationship between the fusion results and the input images, and temporal consistency loss, which enhances the temporal correlation in the fused outputs. This approach was tested on both surface reflectance bands and LST.

Table IV provides an overview of DL-based STF methods, comparing them across eight key criteria. The comparison includes the types of satellites employed (*Satellites*). It also considers whether the methods were validated on LST data (*LST*), the number of temporal pairs needed to generate HSHT images (*Pairs*), and the resizing strategies applied to align spatial resolutions (*Resizing*). Furthermore, it outlines the loss functions utilized for optimization (*Loss Function*), the performance metrics reported (*Metrics*), the source of the datasets, whether pre-existing or handcrafted (*Dataset*), and the availability of implementation code for reproducibility (*Code Source*). From Table IV, it is evident that most CNN-based STF methods were designed for MODIS and Landsat satellite data, reflecting the popularity and complementary nature of these datasets for fusion tasks. A significant number of methods, such as those by [39], [66], and [65], utilize two temporal pairs for prediction, which seems to be a prevalent strategy. In contrast, a few approaches, like that of [64], rely on a single temporal pair. Resizing images is a critical preprocessing step, with methods often employing spatial interpolation techniques to ensure the MODIS images match the finer spatial resolution of Landsat. Common interpolation strategies include bicubic, bilinear, and nearest-neighbor methods. The most frequently used loss function for optimization is content loss. In terms of datasets, many studies relied on handcrafted datasets, which highlights the necessity for custom data preparation in this field. Only a few methods, such as that of [64], provide open-source code, which underscores a gap in reproducibility. The methods tested on LST data remain limited, with [67] and [71] being notable exceptions. This indicates an open room for further exploration and validation of STF approaches for thermal remote sensing applications.

2) *Autoencoder*: An AE is an unsupervised learning neural network designed to learn efficient and informative representations of input data [150]. It consists of two main components: the *encoder*, which transforms the input data into a compressed, high-level feature representation, and the *decoder*, which reconstructs the original input from this compact representation [151], [152]. The objective of an AE is to minimize the difference between the original and reconstructed data [153], which enables it to extract meaningful, non-linear features and identify patterns without the need for labeled training data [154]. The basic architecture of a standard AE is illustrated in Figure 7. It consists of three main components: an input layer, a hidden layer, and an output layer. The hidden layer acts as a bottleneck with fewer neurons, forcing the model to learn a compact input data representation [155]. The encoder network maps the input  $X$  to a latent representation  $H$  using an encoding function,  $f_\theta$ . The decoder network then reconstructs the original input,  $X'$ , from  $H$  using a decoding function,  $g_\theta$ , as described in Equation 15 [153].

$$\begin{aligned} H &= f_\theta(X) = s(WX + b) \\ X' &= g_\theta(H) = s(W'H + b') \end{aligned} \quad (15)$$

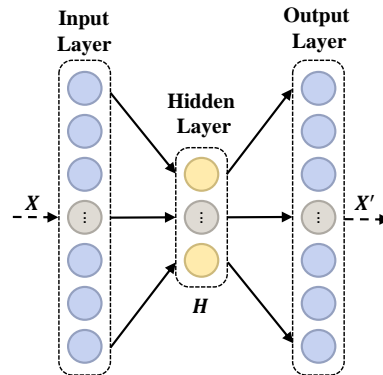


Fig. 7. Basic architecture of a standard AE, consisting of an encoder layer, a hidden layer representing the latent space, and a decoder layer for reconstruction.

where  $s$  is a non-linear activation function such as sigmoid or ReLU.  $W$  and  $W'$  represent the weight matrices, while  $b$  and  $b'$  denote the bias vectors. The autoencoder adjusts these weights and biases during training to minimize the reconstruction error explained in Equation 16 [156].

$$\min_{\theta} J_{AE}(\theta) = \min_{\theta} \sum_{i=1}^n l(x_i, x'_i) = \min_{\theta} \sum_{i=1}^n l(x_i, g_{\theta}(f_{\theta}(x_i))) \quad (16)$$

where  $x_i$  and  $x'_i$  denote, respectively, the  $i$ -th dimension of the input data and its reconstructed output. The parameter  $n$  represents the total number of samples in the training dataset. The term  $l$  signifies the reconstruction error between the original and reconstructed data, previously defined in Equation 10. Stacked AE (SAE) enhance the capability of traditional AE by stacking multiple encoding and decoding layers. This layer-wise approach allows for deeper networks, improving

TABLE IV  
A COMPARATIVE STUDY OF DL-BASED STF METHODS, CATEGORIZED BY MODEL ARCHITECTURE. ROW COLORS REPRESENT DIFFERENT STF METHODS: YELLOW FOR CNN-BASED, ORANGE FOR AE-BASED, GREEN FOR GAN-BASED, BLUE FOR TRANSFORMER-BASED, AND PURPLE FOR RNN-BASED METHOD

Method	Satellites	LST	Pairs	Resizing	Loss Function	Metrics	Dataset	Code
[39]	MODIS, Landsat	✗	2	✗	Content	RMSE, ERGAS, SAM, SSIM	CIA, LGC	✗
[64]	MODIS, Landsat	✗	1	✗	Content	RMSE, $R^2$ , SSIM	Hand-crafted	✓
[65]	MODIS, Landsat	✗	2	✗	Content	RMSE, CC, SSIM	Hand-crafted	✗
[66]	MODIS, Landsat	✗	2	✓	Content	RMSE, SAM, SSIM, ERGAS	CIA, LGC	✗
[67]	MODIS, Landsat	✓	2	✓	Content	RMSE, SSIM	Hand-crafted	✗
[68]	MODIS, Landsat	✗	2	✓	Content	RMSE, CC, UIQI	Hand-crafted	✗
[69]	MODIS, Landsat	✗	2	✗	Content	RMSE, CC, ERGAS, SSIM, SAM	CIA, LGC	✗
[70]	MODIS, Landsat	✗	2	✗	Content, Vision	RMSE, $R^2$ , MAE, rMAE, MAEC	Hand-crafted	✓
[72]	MODIS, Landsat	✗	2	✓	Content, Vision	RMSE, SAM, SSIM	CIA, LGC	✗
[71]	MODIS, Landsat	✓	$n$	✗	Content, Adversarial	RMSE, SSIM, ERGAS, PSNR, SAM	Hand-crafted	✗
[149]	Landsat, Sentinel-2	✗	1	✓	Content	RMSE, CC, SSIM	Hand-crafted	✗
[73]	MODIS, Landsat	✗	2	✓	Content, Feature, Vision	RMSE, SAM, ERGAS	Hand-crafted	✓
[63]	MODIS, FY-4A	✓	2	✗	Content	RMSE, SSIM, LPIPS	Hand-crafted	✗
[75]	MODIS, Landsat	✗	2	✓	Adversarial	RMSE, CC, SSIM, SAM, ERGAS	Hand-crafted	✗
[76]	MODIS, Landsat	✗	2	✓	Content, Adversarial	MAE, RMSE, SSIM, SAM, ERGAS, time	CIA, LGC, Shenzhen	✗
[77]	MODIS, Landsat	✗	1	✓	Content, Spectral, Vision Adversarial	RMSE, SSIM, SAME, $Q_4$	CIA, LGC	✗
[78]	MODIS, Landsat	✗	$\frac{1}{2}$	✓	Content, Feature, Vision, Adversarial	MAE, RMSE, SAM, SSIM	CIA, LGC	✓
[79]	MODIS, Landsat	✗	1	✓	Adversarial	MSE, SSIM, CC, UIQI, ERGAS, SAM	CIA, LGC	✗
[80]	MODIS, Landsat	✗	1	✓	Adversarial, Content, Spectral, Vision	MAE, RMSE, SAM, SSIM	CIA, LGC	✓
[81]	MODIS, Landsat	✗	2	✓	Content, Spectral, Vision, Feature	RMSE, SAM, SSIM, ERGAS	CIA, LGC	✓
[82]	MODIS, Landsat	✗	2	✓	Adversarial, Content, Vision, Spectral	RMSE, SSIM, PSNR, CC	CIA, LGC, Tianjin	✓
[83]	MODIS, Landsat	✗	2	✓	Content	RMSE, SSIM, CC, SAM, ERGAS	CIA, LGC, E-SMILE	✓
[84]	MODIS, Landsat	✗	2	✓	Content	RMSE, MSE, CC, SAM, SSIM, ERGAS, PSNR	CIA, LGC, AHB	✗
[85]	MODIS, Landsat	✗	2	✓	Feature(x)	RMSE, SSIM, ERGAS, SAM, CC	CIA-LGC, DX	✗
[86]	MODIS, Landsat	✗	1	✓	Content, Vision	RMSE, CC, SAM, SSIM, UIQI	CIA-LGC	✓
[87]	MODIS, Landsat	✗	1	✓	Content	RMSE, MSE, CC, SAM, SSIM, ERGAS, PSNR	CIA-LGC, AHB	✓
[74]	MODIS, Landsat	✗	2	✓	Content	MAE, SAM, SSIM, PSNR	CIA, DX	✗
[88]	Planetscope, Pléiades	✗	$\frac{1}{2}$	✓	Content, Vision	RMSE, CC, SAM, SSIM, UIQI	Hand-crafted	✗
[89]	MODIS, Landsat	✗	2	✓	Content	RMSE, ERGAS, SAM	Hand-crafted	✗
[72]	MODIS, Landsat	✗	2	✓	Content, Vision	RMSE, SAM, SSIM	CIA, LGC	✗
[90]	MODIS, Sentinel	✗	$n$	✓	Content	RMSE, SSIM	Hand-crafted	✗

the ability to learn complex and hierarchical features from the data [157], [158].

AE research is rapidly advancing with a range of specialized variants to address specific challenges. Regularized AE refine data representations with constraints like sparsity and orthogonality, as seen in Sparse [159] and Contractive [160] AE. Robust AE, such as Denoising [161] and  $L_{2,1}$  robust AE [162], improve noise handling. Generative AE like Variational [163] and Adversarial AE [164] focus on data generation. Convolutional AE, such as Convolutional variational AE [165], target image tasks. Recurrent AE, including LSTM [166] and GRU [167], are useful for time-series modeling. Semi-supervised AE, such as Semi-supervised variational AE [168]

and Disentangled variational AE [169], leverage both labeled and unlabeled data. Graph AE, including Variational graph AE [163] and Adversarial AE [164], focus on graph data. Finally, Masked AE like Graph masked [170] and Contrastive masked AE [171] are designed for sequence modeling.

AE-based STF techniques efficiently model both spatial and temporal information to establish non-linear relationships between LSHT and HSLT image pairs. While AE are traditionally used for unsupervised learning, in STF they are modified for supervised tasks. The adapted architecture employs an *encoders-merge-decoder* design, as illustrated in Figure 8. Specifically, a spatial feature encoder processes the high-resolution image, transforming it into a latent representation

$H_1$ . Concurrently, a temporal variation encoder compresses two low-resolution images into  $H_2$ . These latent representations,  $H_1$  and  $H_2$ , are then merged using a tailored fusion mechanism to capture the intricate spatio-temporal dependencies. The merged representation is decoded to reconstruct the fused high-resolution image,  $\hat{X}_2$ , which is then compared to the true high-resolution target,  $X_2$ , to compute the loss. This architecture is presented in Figure 8.

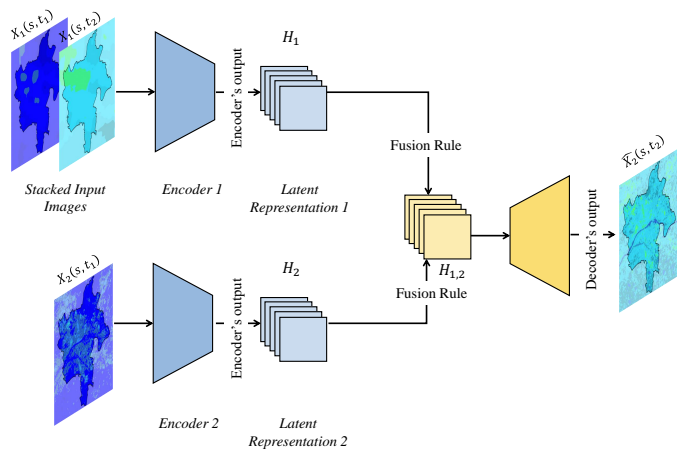


Fig. 8. Typical architecture of an AE-based STF method using a single pair of LST data  $P_1$ . It consists of two encoders: a spatial feature encoder and a temporal variation encoder, along with a decoder. The fusion occurs between the latent representations of the outputs from both encoders. The fusion rule can be Element-wise Addition, Multiplication, Concatenation, Attention, etc.

In [73], the authors proposed an STF method using a basic AE, called EDCSTFN. They introduced a novel compound loss function that combines content, feature, and vision loss components. The method involved resizing MODIS images to match the spatial resolution of Landsat images using spatial interpolation before training. [63] utilized a Conditional Variational AE (CVAE) for STF of LST data. The encoder employed a multi-kernel convolutional transformer to extract global features, while the decoder compressed the fused features using a simple convolutional design. The model included a compound loss function that integrated variational inference and noise mitigation to improve robustness against outliers and ensure high-quality reconstruction. It should be noted that GAN-based AE are better categorized under GAN models for a more accurate comparison, which is why they are not included in this autoencoder category.

Table IV presents a comparative overview of AE-based STF methods. These methods primarily focus on fusing MODIS and Landsat satellite data. A common strategy involves using two temporal pairs for prediction, as demonstrated by [73], [63], and [74]. Resizing of MODIS images is often employed, typically using spatial interpolation to match the finer spatial resolution of Landsat. Open-source code availability remains limited, with [73] being the only study to provide accessible implementations. Moreover, testing on LST data is still scarce, with notable exceptions being the works of [63].

3) *Generative Adversarial Networks*: GANs are a powerful class of machine learning models that facilitate unsupervised

learning by generating synthetic data closely resembling real-world data [124]. At the core of GANs are two neural networks: the Generator and the Discriminator [172]. The Generator creates artificial data, while the Discriminator evaluates whether it is real or fake, based on its resemblance to real samples [173]. Through a competitive process, in which the Generator continuously improves its ability to create realistic data, and the Discriminator refines its ability to distinguish real from fake, the two networks engage in a dynamic adversarial game [174]. Over time, this iterative learning process allows the Generator to produce compelling outputs, often indistinguishable from real data. GANs have been successfully applied to various domains, including image generation [175], super-resolution [176], denoising [177], and image-to-image translation [178]. The basic architecture of a standard GAN is illustrated in Figure 9.

The loss function used for the Discriminator is derived from the binary cross-entropy formula, which is formulated in equation 17 [179].

$$L(\hat{y}, y) = [y \cdot \log(\hat{y}) + (1 - y) \cdot \log(1 - \hat{y})] \quad (17)$$

where  $y$  and  $\hat{y}$  correspond to the original and fake data, respectively.

In the training of  $D$ , the real data  $\mu(x)$  is assigned a label  $y = 1$  (real data), and the output of the Discriminator for real data is  $\hat{y} = D(x)$ .  $\mu$  denotes the true, real data distribution from which the training dataset is sampled. Substituting this into Equation 17, we get the loss defined in Equation 18.

$$L(D(x), 1) = \log(D(x)) \quad (18)$$

For data sampled from  $G$ , the assigned label is  $y = 0$  (fake data), and the predicted output is given as  $\hat{y} = D(G(z))$ . By substituting these values into Equation 17, the resulting expression is defined in Equation 19.

$$L(D(G(z)), 0) = \log(1 - D(G(z))) \quad (19)$$

The discriminator's objective is to classify its input accurately as either fake or real. Consequently, the associated loss functions for  $G$  and  $D$  must be optimized. The final loss function of  $D$  is expressed in Equation 20.

$$L^{(D)} = \max[\log(D(x)) + \log(1 - D(G(z)))] \quad (20)$$

The generator's objective is to compete against the discriminator by minimizing the optimization problem. Accordingly, the generator's loss function is formulated in Equation 21.

$$L^{(G)} = \min[\log(D(x)) + \log(1 - D(G(z)))] \quad (21)$$

By combining the loss functions of the generator and discriminator, we can frame the optimization as a min-max problem. This is expressed in Equation 22.

$$L = \min_G \max_D [\log(D(x)) + \log(1 - D(G(z)))] \quad (22)$$

The loss function in Equation 22 applies only to a single data point. To extend it to the entire dataset, the expectation of the combined loss is considered, as presented in Equation 23.

$$\min_G \max_D V(D, G) = \min_G \max_D \left[ \mathbb{E}_{x \sim \mu} [\log(D(x))] + \mathbb{E}_{z \sim \gamma} [\log(1 - D(G(z)))] \right] \quad (23)$$

This min-max formulation concisely captures the adversarial competition between the generator  $G$  and discriminator  $D$ . However, in practice, distinct loss functions are defined for both players. This adjustment arises because the gradient of  $y = \log(x)$  is steeper near  $x = 0$  compared to  $y = \log(1 - x)$ . Consequently, minimizing  $-\log(D(G(z)))$  accelerates generator improvement more effectively than minimizing  $\log(1 - D(G(z)))$ .

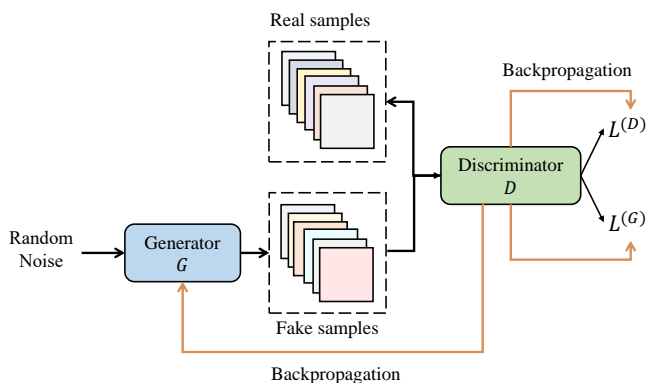


Fig. 9. Basic architecture of a standard GAN, comprising a generator that produces data and a discriminator that evaluates its authenticity.

GANs have undergone significant evolution, with multiple variants adapting the original architecture for various tasks. Initially, Fully Connected GANs used simple neural networks for both the generator and discrimination [124]. Convolutional GANs (CGANs) extended this framework by incorporating convolutional layers, which are more suitable for image generation. LAPGAN [180] and DCGAN [181] as examples of CGANs architectures. Conditional GANs (cGANs) further enhanced GANs by conditioning the generator and discriminator on additional information, such as class labels, which allows more controlled generation of data. An example of cGANs are InfoGAN [182] and [183]. GANs with Inference Models introduce mechanisms to map observed data to latent vectors, as seen in ALI [184] and BiGAN [185]. Lastly, Adversarial Autoencoders (AAEs) combine the principles of autoencoders with adversarial loss, as seen in VAE [186] and AVB [187], to improve generative capabilities.

GAN-based STF models consist of two primary components, as presented in 10: the generator and the discriminator. The generator is tasked with creating high-resolution fused images by leveraging input pairs from either a single pair or two temporal pairs ( $P_1$  and  $P_3$ ). The discriminator evaluates the outputs by distinguishing between real high-resolution images and those generated by the model (the fused image).

cGANs are most commonly employed for STF, as they allow conditioning the generation process on low-resolution input images to preserve temporal and spatial consistency. The generator operates in three stages: feature extraction, feature fusion, and image reconstruction. The encoding-decoding framework is central to enhancing spatial resolution during feature extraction and reconstruction, while the feature fusion stage integrates the extracted features to synthesize temporally consistent outputs. The discriminator takes as input both the coarse-resolution image at the target date and either the real or predicted fine-resolution image. It is trained to output probabilities indicating whether the input is real (ground truth) or synthetic (generated), and thus, by using a sigmoid activation function in the final layer. During training, when the discriminator receives real pairs (real fine-resolution and coarse-resolution LST images), it is expected to classify them as true (1). When presented with synthetic pairs (predicted fine-resolution and coarse-resolution LST images), it learns to classify them as false (0).

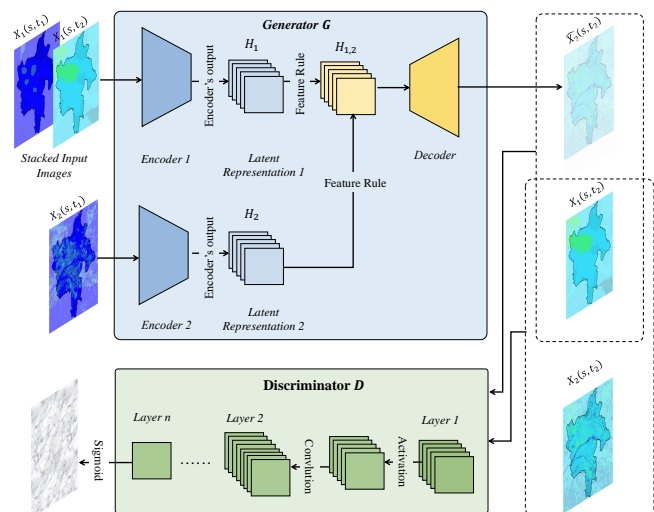


Fig. 10. Typical architecture of a GAN-based STF method. It consists of a generator that creates high-resolution fused images using input pairs and a discriminator that distinguishes between real and generated fine-resolution images. The generator includes feature extraction, fusion, and image reconstruction stages, while the discriminator evaluates temporal and spatial consistency.

In [75], the authors proposed a Cycle-GAN-based STF method to model temporal transitions between HSLT images at  $k - 1$  and  $k + 1$ . By generating intermediate images, the approach effectively captures temporal dynamics. These results are further refined using wavelet transforms. [76] proposed a two-stage GAN-based STF framework. The generator utilizes a residual-block architecture for high-frequency feature extraction, combined with a feature-level fusion strategy to integrate these extracted features effectively. Their approach was evaluated on three diverse Landsat–MODIS datasets: CIA, LGC [148], and Shenzhen datasets. [77] proposed an STF model that separately models spatial, sensor, and temporal differences in satellite images using deep neural networks. The spatial difference is handled through cascaded dual regression networks, the sensor difference through four-layer CNNs, and

the temporal difference using a GAN [78] introduced a GAN-based spatiotemporal fusion model that simplifies STF by requiring only two inputs: a coarse-resolution image from the prediction date and a fine-resolution reference image from any prior time. This model integrates a CGAN to perform the fusion. [79] developed a GAN-based STF model that utilizes advanced segmentation methods and a linear injection model to improve prediction accuracy, particularly in regions with minimal shape changes, such as phenological shifts or land cover changes. [80] proposed a U-net-like architecture, named MLFF-GAN, with a generator composed of three stages: feature extraction, feature fusion, and image reconstruction. The model addresses resolution discrepancies by extracting multi-level features through encoding and decoding structures, using Adaptive Instance Normalization for global feature fusion, and an attention module to adapt to local changes. [81] introduced a GAN-based model with an attention mechanism to handle noisy input data in STF tasks. It utilizes one coarse-resolution image from the prediction date and two fine-resolution reference images from before and after the prediction date. [82] advanced the GAN-based STF methods by introducing an adaptive multiscale pyramidal architecture, which incorporates deformable convolutions and an adaptive attention module. Extensive evaluations on CIA [148], LGC [148], and Tianjin [94] datasets. [83] presented a diffusion-based method that generates high-resolution satellite images by refining a noisy initialization iteratively. The method incorporates a dual-stream Unet (DS-Unet) architecture for conditional noise prediction, extracting features from both coarse and fine images to reduce noise and generate high-resolution images with accurate spatial details and temporal dynamics. The method was evaluated on the CIA [148], LGC [148], and E-Smile [188] datasets.

Table IV provides a summary of GAN-based STF methods. Most methods rely on two temporal pairs for predictions, though some, such as [77] and [79], utilize a single pair. Resizing of MODIS images to match Landsat’s finer resolution is a common preprocessing step. Loss functions often combine GAN-specific losses with additional terms like content, spectral, and perceptual losses to enhance reconstruction quality and spatial fidelity. Compared to other techniques, GAN-based methods exhibit broader availability of open-source implementations, with studies like [78], [80], and [82] sharing accessible code. This accessibility fosters reproducibility and further development. However, none of these methods have been tested on LST data, which presents an opportunity for novel contributions in this domain.

4) *Vision Transformers*: Transformer-based models were initially developed for natural language processing to model sequential dependencies through self-attention mechanisms [189], achieving remarkable success in tasks like machine translation and text generation [190]. This success inspired [191] to adapt Transformers to CV, proposing the Vision Transformers (ViTs), which redefined feature extraction in image tasks [139], [192]. In ViTs, images are split into fixed-sized patches, flattened into vectors, and passed through a linear projection to create patch embeddings. Positional

embeddings have been added to retain spatial information. The embeddings are processed through a Transformer encoder, consisting of multi-head attention and feed-forward layers, with skip connections and LayerNorm to ensure stability. A final MLP Head maps the output to predictions. When trained on large datasets like JFT-300M [193], ViT outperformed convolutional architectures like ResNets [194].

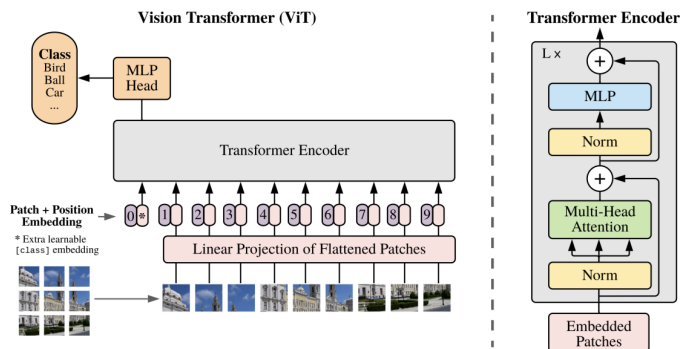


Fig. 11. Basic architecture of a ViT [191].

In a self-attention layer, the input vector  $X$  is initially transformed into three distinct vectors: the query vector ( $Q$ ), the key vector ( $K$ ), and the value vector ( $V$ ). These vectors are of fixed dimensions and are generated by multiplying the input with corresponding learnable weight matrices, denoted as  $W_Q$ ,  $W_K$ , and  $W_V$ . Mathematically, this process is expressed as in Equation 24.

$$Q = W_Q X, \quad K = W_K X, \quad V = W_V X \quad (24)$$

where  $W_Q$ ,  $W_K$ , and  $W_V$  are learnable parameters.

Once these vectors are obtained, the scaled dot-product attention mechanism is applied to compute the attention scores, as shown in Equation 25.

$$\text{Attention}(Q, K, V) = \text{Softmax} \left( \frac{QK^\top}{\sqrt{d_k}} \right) V \quad (25)$$

where  $d_k$  represents the dimensionality of the key vector, and its square root is used to improve gradient stability. The  $\text{Softmax}$  function normalizes the attention weights and converts them into a probability distribution.

While a single self-attention mechanism effectively models dependencies between token entities, it may lack the capacity to capture complex relationships from diverse perspectives. To address this limitation, the multi-head self-attention mechanism (Figure 12 (b)) was introduced by [189]. It allows the model to attend to the information from multiple representation sub-spaces jointly. Mathematically, this process is expressed as in equation 26.

$$\text{MultiHead}(Q, K, V) = \text{Concat}(\text{head}_1, \dots, \text{head}_h) W_O \quad (26)$$

$$\text{head}_i = \text{Attention}(QW_Q^i, KW_K^i, VW_V^i)$$

where  $W_O$  denotes a linear mapping function used to combine the multi-head representations. Here,  $h$  is a hyperparameter

representing the number of heads, which is set to  $h = 8$  in the original work [189].

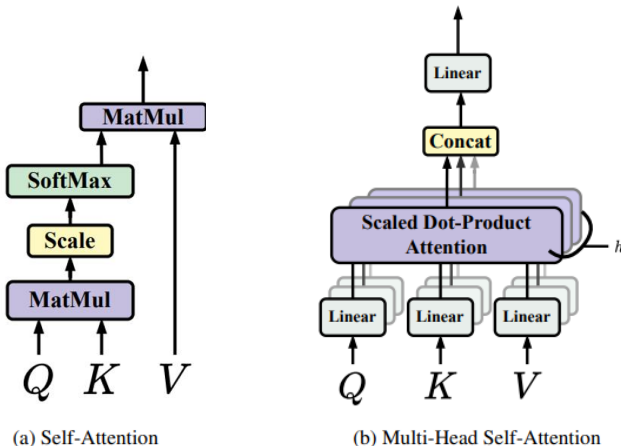


Fig. 12. (a) The process of self-attention. (b) Multi-head attention [189].

Since the inception of transformers, several variants have been proposed to enhance its performance. These include DeiT [195], which utilized knowledge distillation, TNT [196], which incorporated token mixing, and PVT [197], which introduced a pyramid vision transformer to better handle varying scales. Although ViT uses a patchification strategy that might miss finer local image details, the Shifted Windows Transformer (Swin) [198] overcomes this drawback by incorporating a shifted window approach to effectively capture global and boundary features. Likewise, Twins [199] implemented a spatially separable self-attention mechanism to capture both local and global context. ViL [200] replaced the traditional single class token with multiple local embeddings that perform internal attention and interact with their neighboring 2D spatial regions. VOLO [201] introduced outlook attention, which refines the model’s ability to capture finer details by utilizing processes such as unfolding, applying linear weights, and refolding.

Transformer-based STF models typically consist of two main components: the transformer encoder and the transformer decoder, as illustrated in 13. The process begins by dividing each input image into a sequence of patches. These patches, along with their respective positional embeddings, are then fed into the transformer encoder. In particular, a spatial feature transformer encoder processes the high-resolution image, while a temporal transformer encoder compresses the two low-resolution images. Both encoders output a sequence of patches, which are subsequently fused and passed through the transformer decoder along with their respective positional embeddings. The transformer decoder then generates a sequence of patches, which, after reshaping, are used to produce the final predicted high-resolution image.

In [84], the authors introduced a multi-stream STF method combining transformers with CNNs to capture global temporal correlations to capture global temporal correlations while focusing on feature extraction. It was tested on LGC, CIA [148], and AHB [94] datasets. Bilinear interpolation was applied

for size matching between MODIS and Landsat images. [86] proposed an STF method based on the Swin Transformer and integrated linear spectral mixing theory. [87] enhanced STF by incorporating an improved transformer encoder and dilated convolutions to expand the receptive field. [85] introduced MSFusion, which employs a texture transformer for STF. [74] developed an AE model with a multi-kernel convolutional transformer encoder for global feature extraction. [88] proposed STF-Trans, a transformer-based STF method that uses only one high-resolution image at any arbitrary date alongside coarse-resolution temporal data. It employs an encoder-decoder transformer architecture for efficiently capturing long-range dependencies.

Table IV summarizes recent transformer-based methods for STF. Most of these methods began emerging around 2021, a trend justified by the advent of ViTs in 2020. The majority of these methods employ simple preprocessing techniques, such as resizing MODIS images to match Landsat’s resolution. Loss functions typically emphasize content preservation, with some methods incorporating additional vision-based losses for enhanced fusion quality. Open-source implementations are available for some methods, like [86] and [87]. The advances in these transformer models underscore their promising potential in STF tasks, especially with the increasing application of transformers in CV tasks.

5) *Recurrent Neural Networks*: RNN are a class of supervised machine learning models designed to process sequential or time-series data [150]. They incorporate feedback connections that allow outputs from previous steps to be used as inputs for the current step [202]. This recurring process of utilizing feedback connections gives the network its name and helps it to retain information from past inputs through a hidden state [203]. At each time step  $t$ , an RNN processes an input vector  $\mathbf{x}_t$  and updates its hidden state  $\mathbf{h}_t$ , as shown in equation 27. The basic architecture of a standard RNN is illustrated in Figure 14.

$$\mathbf{h}_t = \sigma_h (\mathbf{W}_{xh}\mathbf{x}_t + \mathbf{W}_{hh}\mathbf{h}_{t-1} + \mathbf{b}_h), \quad (27)$$

where  $\mathbf{W}_{xh}$  is the weight matrix mapping the input to the hidden layer,  $\mathbf{W}_{hh}$  is the weight matrix representing the recurrent connection,  $\mathbf{b}_h$  is the bias term, and  $\sigma_h$  is the activation function, typically chosen as the hyperbolic tangent (tanh) or RELU [204], [205]. The output at time step  $t$  is computed according to equation 28.

$$\mathbf{y}_t = \sigma_y (\mathbf{W}_{hy}\mathbf{h}_t + \mathbf{b}_y), \quad (28)$$

where  $\mathbf{W}_{hy}$  denotes the weight matrix connecting the hidden and output layers,  $\mathbf{b}_y$  is the bias term for the output layer, and  $\sigma_y$  is the activation function applied at the output.

RNNs have many variants that address their limitations and expand their capabilities. Long Short-Term Memory networks (LSTMs) [206] introduced gating mechanisms to overcome the vanishing gradient problem and better model long-term dependencies. Bidirectional LSTMs [207] process sequences in both forward and backward directions to capture context from past and future tokens. Stacked LSTMs [208] stack multiple

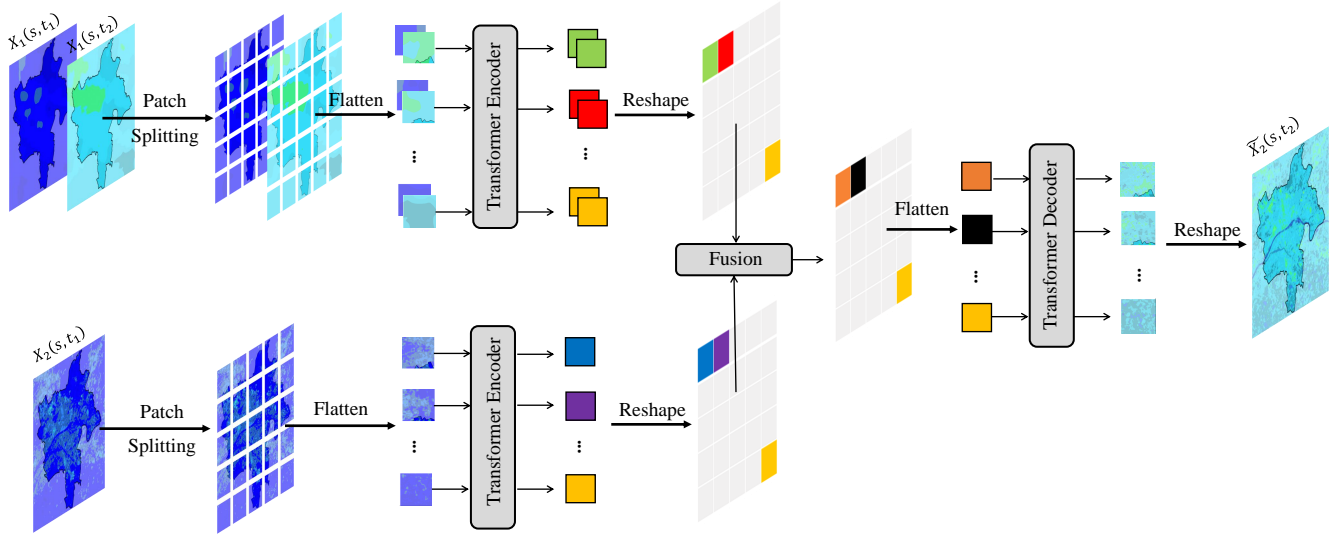


Fig. 13. Typical architecture of a Transformer-based STF method. It consists of a spatial feature transformer encoder for high-resolution input, a temporal transformer encoder for low-resolution inputs, and a transformer decoder for generating high-resolution output. The method processes images as patch sequences with positional embeddings.

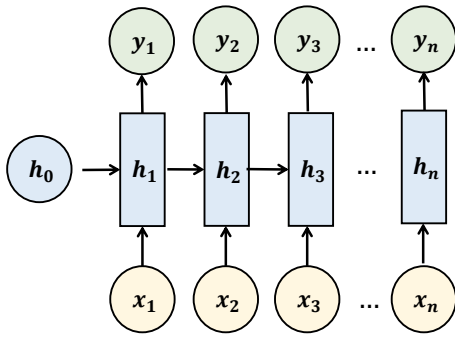


Fig. 14. Basic architecture of a RNN.  $x_t$  represents the temporal input data at time  $t$ ,  $y_t$  denotes the output at time  $t$ , and  $h_t$  indicates the hidden state at time  $t$ .

layers of LSTMs to learn hierarchical patterns in data. Gated Recurrent Units (GRUs) [209] simplify LSTM architecture by combining certain gates which reduces complexity while retaining effectiveness. Other RNN variants include Peephole LSTMs [210], Echo State Networks [211], and Independently Recurrent Neural Networks [212].

In RNN-based STF, the goal is to leverage temporal dependencies between coarse and fine-resolution images. For a given set of  $n$  pairs,  $P_i$ , we train a RNN to learn the temporal relationships and map coarse-resolution input data to fine-resolution predictions. Specifically, the RNN is trained to predict the fine-resolution image at time step  $t_i$ , denoted as  $X_2(s, t_i)$ , where  $i \in [1, n]$ . Once trained, the model is used to generate fine-resolution estimates for  $X_1(s, t_1)$ ,  $X_1(s, t_2)$ , and  $X_1(s, t_3)$ . Subsequently, these predicted fine-resolution outputs are combined with the original coarse-resolution data,  $X_2(s, t_1)$  and  $X_2(s, t_2)$ , to generate the final fused image.

In [89], the authors proposed a hybrid deep learning model

combining a Super-Resolution CNN and an LSTM for STF. The first component focuses on enhancing spatial resolution by recovering fine details, while the LSTM captures temporal patterns in time-series data, which is critical for modeling rapid and transient phenological changes. However, their approach processes only pixel-level data with six bands, which potentially limits its ability to fully exploit the spatial context of remote sensing images. [90] advanced this concept by integrating a UNet for spatial mapping between MODIS and Sentinel-2 images with an LSTM to capture temporal dynamics. Using multi-temporal MODIS-Sentinel-2 NDVI pairs from previous years, their architecture generates higher-resolution NDVI data during key crop growth periods.

Table IV summarizes recent RNN-based methods for STF. RNNs are the least popular architecture for STF, as AE are commonly integrated within most GAN and transformer-based approaches. This is primarily because RNNs are more suited for sequential, vector-type data, whereas STF tasks benefit more from the spatial and temporal capabilities of CNNs, GANs, and transformers.

## B. Learning Algorithms

Various types of learning algorithms have been integrated into STF frameworks, and they are generally classified into four categories: *supervised*, *unsupervised*, *self-supervised*, and *collaborative learning*.

1) *Supervised Learning*: Supervised learning involves training a model on labeled data, where the input data is paired with corresponding output labels [213]. In STF, this means that  $X_2(s, t_i)$  is known. Most approaches listed in IV rely on supervised learning.

2) *Unsupervised Learning*: Unsupervised learning consists of training a model on input data without labels, where the algorithm must identify patterns within the data [213]. In STF,



this means that  $X_2(s, t_i)$  is unknown. Only one recent work has explored this research direction [149].

3) *Self-supervised Learning*: Self-supervised learning is considered to be the bridge between supervised and unsupervised learning, where the model generates its own labels from the data itself [213]. Only one study has explored this category [71].

4) *Collaborative Learning*: Collaborative learning is an approach in which groups of learners work together to solve a problem [214]. In STF, the problem is the fusion task. Only one study has viewed the STF problem as a collaborative process [72].

### C. Training Strategy

Training strategies refer to the techniques used to enhance the performance of a neural network during the training process. These strategies are employed in STF methods and can be categorized into four main classes: *Residual Learning*, *Attention mechanisms*, *Normalization*, and *Dropout*.

1) *Residual Learning*: Residual learning, first introduced [144] for image recognition tasks, is a technique designed to address the challenges of vanishing and exploding gradients in training deep neural networks. The idea behind residual learning is the introduction of skip connections, which directly add the input from a previous layer to the output of the current layer [215]. This allows the network to learn residual mappings, rather than the original function itself, which makes it easier for deep networks to converge during training and prevents degradation in performance as the network depth increases [216]. Mathematically, it can be defined as described in Equation 29.

$$F(x) := H(x) - x \quad (29)$$

where  $H(x)$  is the desired underlying function, and  $F(x)$  is the residual mapping. Thus, the final output of a residual learning block is  $F(x) + x = H(x)$ . In STF, residual learning is widely used to preserve important spatial and temporal features while reducing computational complexity [217]. Based on Table V, it is evident that residual learning is the most commonly adopted training strategy in STF methods. The extensive use of residual learning in various approaches highlights its importance in improving model convergence, preserving critical spatial and temporal features, and mitigating computational complexity.

2) *Attention Mechanism*: Attention mechanisms in DL focus on identifying and prioritizing the most relevant parts of the input for a specific task, as previously described in Section IV-A4. In STF, attention mechanisms have been applied in four levels: *channel attention*, *spatial attention*, *temporal attention*, and *feature attention*. *Channel attention* prioritizes specific spectral bands, but it is less applicable to LST data, which typically consists of a single band. *Spatial attention* focuses on identifying critical regions within the spatial domain. *Temporal attention* captures significant changes across time. *Feature attention* evaluates the importance of entire feature maps. As shown in Table V, all transformer-based STF methods incorporate spatial attention. This is expected, as transformers

rely on attention mechanisms, with spatial attention central to capturing spatial relationships.

3) *Normalization*: Normalization is a transformation applied to ensure that data exhibits specific statistical properties, which can enhance both the training efficiency and the generalization capability of DL [218]. In the literature, normalization typically encompasses five operations: centering, scaling, decorrelating, standardizing, and whitening [218]. For STF, five primary types of normalization are employed: *Batch Normalization (BN)*, *Group Normalization (GN)*, *Instance Normalization (IN)*, *Spectral Normalization (SN)*, and *Switchable Normalization (SwN)*. BN [219] operates over mini-batch inputs to mitigate issues such as internal covariate shift during backpropagation. Given a neuron activation  $a$ , BN standardizes the neuron across  $m$  mini-batch samples as defined in Equation 30.

$$\hat{a}^{(i)} = \frac{a^{(i)} - \mu}{\sqrt{\sigma^2 + \epsilon}} \quad (30)$$

where  $\epsilon > 0$  prevents numerical instability, and  $\mu$  and  $\sigma^2$  denote the mean and variance of the mini-batch, respectively. GN [220] divides neurons into predefined groups and standardizes the activations within each group for individual samples. IN [221] normalizes each image individually, removing instance-specific contrast information. This is particularly beneficial in tasks like style transfer. SN [222] is primarily used in GANs. It stabilizes the training process of the discriminator by normalizing the spectral norm of weight matrices by controlling the Lipschitz constant of the model's layers. SwN [223] combines three types of statistics: channel-wise, layer-wise, and mini-batch-wise. Table V classifies each DL-based method into its respective normalization category.

4) *Dropout*: Dropout is a regularization method that helps reduce overfitting by randomly deactivating neurons of the neural network during training [224]. As presented in Table V, dropout in STF is not that much popular, with only five works applying it, but it's still an interesting research direction.

### D. Incorporation of Pre-trained Models

DL models typically involve many parameters, which can lead to overfitting when trained on small datasets, and result in poor generalization [225]. Many DL tasks are also interrelated, making pre-train models on other datasets beneficial [226]. The effectiveness of pretraining was first demonstrated in the field of CV by [142].

Pretraining offers a promising solution for STF methods by addressing three challenges. First, STF-specific data is often limited. This is due to the acquisition of pairs of coarse and fine resolution images captured simultaneously for the same region. This requirement for temporal and spatial alignment reduces the number of available pairs significantly, as both datasets must overlap in time and coverage. For instance, the CIA dataset includes only 17 pairs, while the LGC dataset contains just 14 pairs [148]. Furthermore, external factors, such as weather conditions, can introduce inconsistencies, further complicating data distribution and reducing the amount

TABLE V  
CATEGORIZATION OF DL-BASED STF METHODS BASED ON THEIR TRAINING STRATEGIES, GROUPED INTO FOUR CATEGORIES: RESIDUAL LEARNING, ATTENTION MECHANISMS, NORMALIZATION, AND DROPOUT.

Category	Methods
<b>Residual Learning</b>	[39], [66], [67], [68], [69], [71], [73], [63], [76], [77], [78], [80], [81], [82], [83], [84], [87], [74]
<b>Attention Mechanism</b>	<b>Channel Attention:</b> [70], [77], [74] <b>Spatial Attention:</b> [83], [84], [85], [86], [87], [74], [88] <b>Temporal Attention:</b> [79], [80], [81] <b>Feature Attention:</b> [80]
<b>Normalization</b>	<b>Batch Normalization:</b> [39], [67], [70], [63], [76], [77], [78], [81], [82], [90] <b>Group Normalization:</b> [83], [74] <b>Instance Normalization:</b> [80] <b>Spectral Normalization:</b> [77], [78], [81] <b>Switchable Normalization:</b> [77], [78], [85]
<b>Dropout</b>	[82], [84], [87], [89], [90]

of usable training data [226]. These limitations are also prevalent in STF for LST. Second, pretraining provides a strong initialization for the model, which typically leads to improved generalization performance and accelerates convergence on the target task [227]. Third, pretraining can function as a form of regularization, which helps to prevent overfitting [228].

The use of pre-trained models can be applied in two levels: *feature extraction* and *transfer learning*. Table VI provides an overview of STF methods categorized by their use of pre-trained models at each level.

1) *Feature Extraction*: Pre-trained models are utilized solely to extract informative features from the input data, without any additional fine-tuning [229]. In STF, this approach is typically employed to compute feature or spectral loss, as discussed in Section III-B3 and III-B4.

2) *Transfer Learning*: It aims to enhance a learner’s performance in one dataset by leveraging information from a related dataset [230]. In this approach, models are fine-tuned on the target task using a dataset related to the original one, which enables the model to adapt its learned representations to the specific requirements of the new task. Formally, transfer learning is defined as follows [231]: Given a source dataset  $\mathcal{D}_S$  with a corresponding source task  $\mathcal{T}_S$ , and a target dataset  $\mathcal{D}_T$  with a corresponding target task  $\mathcal{T}_T$ , transfer learning seeks to improve the target predictive function  $f_T(\cdot)$  by utilizing related knowledge from  $\mathcal{D}_S$  and  $\mathcal{T}_S$ , where  $\mathcal{D}_S \neq \mathcal{D}_T$  or  $\mathcal{T}_S \neq \mathcal{T}_T$ . The only work explicitly implementing this concept is [63]. They employed a pre-trained AE, where the encoder and decoder networks were initially trained on simulated data to create a pre-training model. The parameters of this model were then transferred as initial values for their fusion framework.

The simulated data were generated by downscaling MODIS LST data to a 4 km resolution, using pixel aggregation via an averaging method. Additionally, [83] addressed the issue of transferability by proposing a fine-tuning strategy to adapt a pre-trained model to a new region or domain. However, their method did not involve using pre-trained models for initial training. Thus, their work is not included under this level.

TABLE VI  
SUMMARY OF STF METHODS UTILIZING PRE-TRAINED MODELS, CATEGORIZED BY FEATURE EXTRACTION AND TRANSFER LEARNING LEVELS.

Level	Methods
<b>Feature Extraction</b>	[73], [77], [78], [80], [81], [82], [85]
<b>Transfer Learning</b>	[63]

## V. EXPERIMENT STUDY

### A. Dataset

The open-source code to generate the dataset is available on GitHub<sup>2</sup>. Please note that you must first authenticate via GEE to download it.

1) *Study Area*: The study area is Orléans Métropole (Figure 15), located in the Centre-Val de Loire region, specifically in the Loiret département of France. Situated between latitudes 47°45’N and 48°0’N and longitudes 1°45’E and 2°7’E, it spans an area of approximately 334.3 km<sup>2</sup> and is crossed by the Loire, France’s longest river. Orléans Métropole encompasses 22 municipalities and has a population of nearly 280,000 habitants, with approximately 115,000 residing in the city center. This makes it one of Europe’s top 140 cities in demographic, economic, and scientific significance. On a national scale, the agglomeration ranked 23rd among France’s main urban units as of 2010. Urban development in Orléans Métropole is characterized by a dense urban fabric in the northwestern part, the city center, and portions of the southern area, primarily comprising built-up plots. The historic core is centered around the cathedral and key arterial roads. In recent decades, urban sprawl has led to the emergence of additional urban centers within the metropolitan area. Climatically, Orléans experiences a temperate oceanic climate with Atlantic influences, featuring cold winters and mild, pleasant summers.

2) *Satellite Data and LST retrieval*: In this study, we use two satellite datasets: MODIS/Terra LST and Emissivity Daily Global 1-km (MOD11A1, Collection 6) for coarse-resolution LST data, and Landsat 8 TM/ETM+ Level 2, Collection 2, Tier 1 for fine-resolution LST data. These datasets were chosen for two main reasons:

- Both MODIS and Landsat 8 observe the Earth in the morning, with overpass times typically between 10:30 AM and 11:00 AM. This temporal consistency ensures that the data from both satellites are captured under similar atmospheric and illumination conditions.

<sup>2</sup>[https://github.com/Sofianebouaziz1/STF-LST\\_Dataset](https://github.com/Sofianebouaziz1/STF-LST_Dataset)

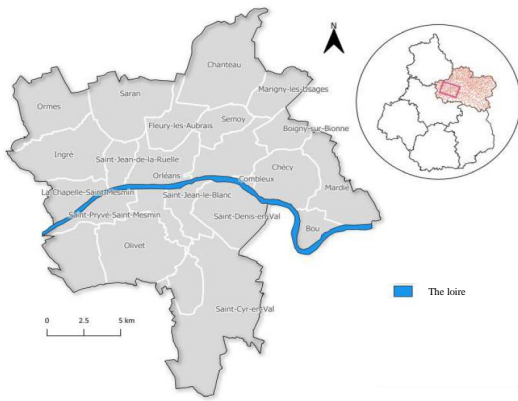


Fig. 15. The geographic location of the study site in Orléans Métropole.

- MODIS provides daily LST data at a coarse spatial resolution of 1 km, while Landsat 8 offers a finer spatial resolution of 30 meters but with a much lower temporal resolution, capturing one image every 16 days. By MODIS and Landsat LST, we can overcome this tradeoff and generate daily LST data at a spatial resolution of 30 meters.

Both MODIS and Landsat 8 datasets were accessed via Google Earth Engine (GEE) [232], which provides pre-corrected data for atmospheric and emissivity effects [233], [234]. MODIS data includes the *LST\_Day\_1km* band, used to derive LST through the Split Window algorithm. This method achieves an RMSE of less than  $2^{\circ}\text{C}$  for most land cover types [235], [236]. Similarly, Landsat 8 data uses the thermal band *ST\_B10* to calculate LST, processed with the Single Channel algorithm and achieves an accuracy within  $1.5^{\circ}\text{C}$  [109].

A total of 51 MODIS-Landsat data pairs were collected for the period between March 18, 2013, and October 15, 2024. To ensure data quality, filtering conditions were applied to both datasets. Only Landsat images with less than 80% cloud cover and MODIS images with less than 90% cloud cover were included in the study. The dataset was divided into three subsets: training, validation, and test sets. Within each subset, overlapping data samples were allowed to maximize the number of training instances. For example, the first training sample consists of data pairs from timestamps  $t_1$ ,  $t_2$ , and  $t_3$ , while the second training sample includes pairs from  $t_2$ ,  $t_3$ , and  $t_4$ , resulting in partial overlap between consecutive samples. However, no overlap was permitted between the training, validation, and test sets. The final distribution of the dataset consists of 34 samples in the training set, each comprising three MODIS-Landsat data pairs. The validation set contains 4 samples, while the test set includes 8 samples.

3) *Data Preprocessing*: Different preprocessing techniques were employed to prepare the data for STF.

First, spatial and linear interpolation were applied for gap filling. For Landsat data, a temporal interpolation was performed using an interval of 32 days, ensuring that two Landsat images before and two after each missing value were used. This approach leverages temporal continuity to reconstruct miss-

ing data, particularly effective for phenomena with gradual changes over time. If gaps persisted after temporal interpolation, a spatial interpolation technique known as the focal mean was applied. This method fills the remaining gaps by averaging the values of neighboring pixels, which ensures smooth and spatially consistent results. For MODIS data, only spatial interpolation using the focal mean was applied to address gaps, as its daily temporal resolution already provides sufficient temporal coverage. Figure 16 illustrates a Landsat LST image of the Orléans Métropole region, acquired on September 30, 2022, shown before and after gap filling.

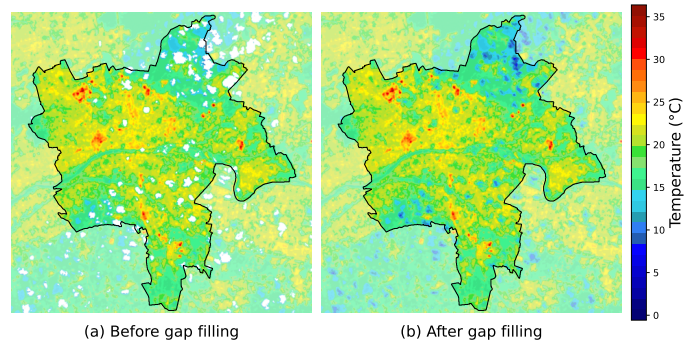


Fig. 16. Comparison of Landsat LST image for Orléans Métropole on September 30, 2022, before and after gap filling.

Second, to harmonize the datasets, MODIS images were resampled to match the spatial resolution of Landsat data using bicubic interpolation. This ensures that the number of pixels in MODIS images aligns with Landsat. Figure 17 demonstrates the result of this resampling for a MODIS LST image acquired on September 30, 2022, for the Orléans Métropole region.

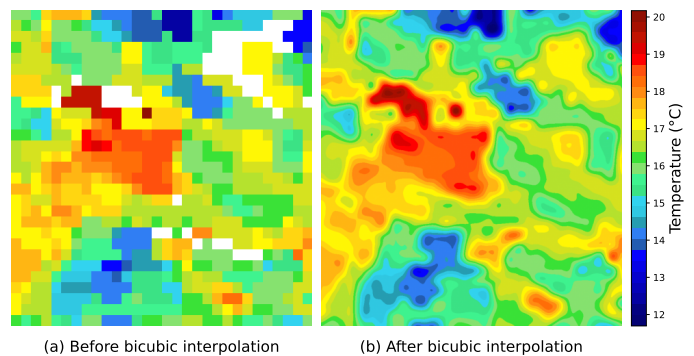


Fig. 17. Comparison of MODIS LST image for Orléans Métropole on September 30, 2022, before and after gap bicubic interpolation.

Finally, to prepare the data for model training, we divided each LST image into smaller patches. Each LST data sample has a spatial size of  $950 \times 950$  pixels. A patch size of  $95 \times 95$  pixels was selected with a stride of 20, resulting in 62,866 training samples and 7,396 validation samples. Using a medium patch size like  $95 \times 95$  strikes a balance between spatial context and computational efficiency. If the patch size were too large, it could capture excessive spatial information, potentially mixing features from heterogeneous land cover types, which might degrade the model's ability to generalize. On the other hand,

if the patch size were too small, it would lack sufficient spatial context, making it challenging for the model to learn meaningful patterns, especially for complex phenomena like LST. Figure 18 represents three random samples derived from the training set after applying the patch division. Each sample consists of three pairs, denoted as  $P_1$ ,  $P_2$ , and  $P_3$ . For the pair  $P_2$ ,  $X_2(s, t_2)$  corresponds to the image we aim to generate or predict.

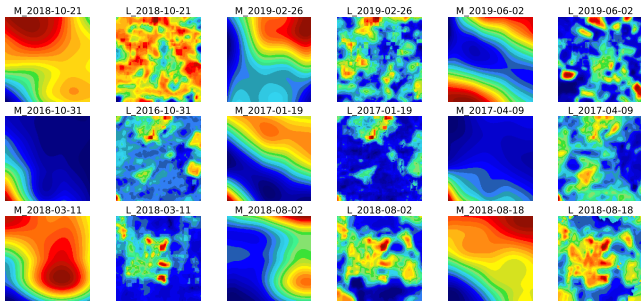


Fig. 18. Example of three random training samples after patch division.

## B. Experimental Results

1) *Comparative algorithms*: In this survey, we evaluate the performance of various STF algorithms on our LST dataset. Several key criteria guided the selection of the comparison algorithms to ensure their relevance to our objectives:

- The chosen algorithms should represent the most current and effective STF approaches by demonstrating strong performance in similar studies and applications.
- The algorithms should be widely recognized and adopted within the RS community.
- The selected algorithms should be supported by open-source implementations, ensuring transparency, reproducibility, and ease of use.

Based on these criteria, we selected four STF methods for comparison:

- ESTARFM [42]: An enhanced weight-based function originally developed for STF of SR. We aim to assess its applicability to LST data.
- STTFN [67]: A CNN-based STF fusion method specifically developed for LST data. We seek to evaluate its performance in complex urban regions like the Orléans Métropole.
- EDCSTFN [73]: An AE-based STF method designed for SR, with the goal of investigating its application to LST data.
- MLFF-GAN [80]: A generative adversarial network (GAN)-based STF method initially developed for SR, which we aim to test on LST data.

This selection covers a broad spectrum of architectures, allowing us to comprehensively assess the effectiveness of STF techniques in LST estimation.

2) *Hyperparameter tuning*: Table VII lists the adjusted hyperparameters used in our study. For the learning rate, we adopted the values provided in the respective articles for each

method. Note that each method has its own unique set of hyperparameters, and wherever possible, we utilized the predefined values specified in the original publications to maintain consistency and fairness in our evaluation.

TABLE VII  
NOTATIONS USED IN STF-PROBLEM FORMULATION.

Hyperparameter	Value
Number of epochs	100
Batch size	32
Training patch size	[95, 95]
Training patch stride	20
Test patch size	[95, 95]
Learning rate	$1.5 \times 10^{-5}$ (STTFN), $10^{-3}$ (EDCSTFN), and $2 \times 10^{-4}$ (MLFF-GAN)

3) *Quantitative Assessment*: We compared the comparative algorithms using six quantitative metrics: RMSE, SSIM, PSNR, SAM, CC, and ERGAS, already defined in Section III-C. Table VIII summarizes the results obtained from these evaluations.

The table highlights key differences in the strengths and weaknesses of the fusion methods. ESTARFM consistently performs worse than DL-based approaches, particularly in terms of RMSE and SSIM. For instance, on 13-08-2022, ESTARFM had the highest RMSE of 5.350, and the lowest SSIM of 0.94, compared to the other methods, which demonstrates its limitations in both visual fidelity and quantitative performance. STTFN, relying solely on content loss, often struggles with visual quality metrics like SSIM and CC. For example, on 13-08-2022, STTFN achieved an SSIM of 0.833, and on 19-09-2024, it dropped further to 0.759. These low SSIM values indicate that STTFN does not adequately preserve the visual content of fused images, which could be problematic for applications requiring high visual fidelity. EDCSTFN, which combines Content, Feature, and Vision losses, provides a more balanced and effective approach. On 13-06-2023, it achieved an RMSE of 1.937, an SSIM of 0.892, and an ERGAS of 1.994, outperforming STTFN in most metrics. This method strikes a good balance between content preservation and visual quality, offering improved performance over STTFN. Similarly, MLFF-GAN, which incorporates Adversarial, Content, Spectral, and Vision losses, excels in reducing RMSE but faces challenges with visual quality, like SSIM and SAM. While MLFF-GAN can generate sharper images based on content and spectral loss, it does not achieve the same level of visual fidelity as EDCSTFN, as evidenced by its lower SSIM values. Clearly, DL-based fusion methods outperform traditional techniques, especially when handling complex image features. For instance, EDCSTFN consistently achieves low RMSE values, such as the RMSE of 2.317 on 13-08-2022, far surpassing ESTARFM's RMSE of 5.350. This demonstrates the significant potential of DL in improving both quantitative and visual image fusion results.

4) *Qualitative Assessment*: Since ESTARFM did not yield favorable results in the quantitative assessment, it is excluded from this section. Figure 19 presents the real image alongside

TABLE VIII  
QUANTITATIVE EVALUATION: THE BEST RESULTS ARE HIGHLIGHTED IN BOLD, WHILE THE WORST RESULTS ARE MARKED IN RED.

Date	Metric	ESTARFM	STTFN	EDCSTFN	MLFF-GAN
13-08-2022	RMSE	<b>5.350</b>	6.258	5.725	5.758
	SSIM	<b>0.94</b>	0.833	0.918	0.872
	PSNR	<b>21.410</b>	20.048	20.821	20.772
	SAM	<b>8.450</b>	9.374	8.812	9.118
	CC	<b>0.640</b>	0.537	0.600	0.537
	ERGAS	<b>5.000</b>	5.850	5.352	5.382
13-08-2022	RMSE	2.650	2.649	<b>2.317</b>	2.549
	SSIM	<b>0.870</b>	0.780	0.862	0.829
	PSNR	22.900	22.894	<b>24.058</b>	23.227
	SAM	6.38	7.661	<b>6.336</b>	6.798
	CC	0.650	0.536	<b>0.669</b>	0.595
	ERGAS	4.730	4.728	<b>4.135</b>	4.550
13-08-2022	RMSE	2.720	2.137	1.579	<b>1.037</b>
	SSIM	<b>0.870</b>	0.685	0.848	0.776
	PSNR	23.190	18.980	20.449	<b>24.098</b>
	SAM	6.500	4.861	<b>2.937</b>	3.666
	CC	<b>0.660</b>	0.644	0.653	0.536
	ERGAS	5.65	4.445	3.283	<b>2.157</b>
28-05-2023	RMSE	<b>2.390</b>	3.213	2.719	3.175
	SSIM	<b>0.880</b>	0.768	0.844	0.730
	PSNR	<b>23.780</b>	21.2	22.651	21.304
	SAM	<b>3.410</b>	4.600	4.043	5.555
	CC	<b>0.900</b>	0.808	0.849	0.719
	ERGAS	<b>2.520</b>	3.396	2.874	3.356
13-06-2023	RMSE	1.950	1.993	<b>1.937</b>	2.710
	SSIM	<b>0.900</b>	0.817	0.892	0.843
	PSNR	26.140	25.936	<b>26.183</b>	23.26
	SAM	<b>3.010</b>	3.414	3.115	3.671
	CC	<b>0.910</b>	0.867	0.890	0.846
	ERGAS	2.000	2.051	<b>1.994</b>	2.789
10-10-2023	RMSE	3.820	<b>1.877</b>	2.842	3.028
	SSIM	0.820	0.845	<b>0.858</b>	0.834
	PSNR	20.970	24.322	<b>24.718</b>	20.166
	SAM	8.470	5.132	5.540	<b>5.131</b>
	CC	0.320	0.452	0.436	<b>0.467</b>
	ERGAS	6.190	<b>3.039</b>	4.602	4.904
12-04-2024	RMSE	4.480	4.365	4.186	<b>4.000</b>
	SSIM	0.800	0.789	<b>0.827</b>	0.806
	PSNR	20.440	20.656	21.014	<b>21.414</b>
	SAM	10.910	<b>8.738</b>	9.702	9.852
	CC	0.430	0.428	<b>0.449</b>	0.410
	ERGAS	6.480	6.313	6.058	<b>5.785</b>
19-09-2024	RMSE	3.890	4.484	<b>3.030</b>	3.281
	SSIM	0.800	0.759	<b>0.833</b>	0.718
	PSNR	<b>20.660</b>	16.923	20.329	19.637
	SAM	9.300	7.480	<b>7.230</b>	7.825
	CC	0.430	0.535	<b>0.595</b>	0.449
	ERGAS	5.460	6.289	<b>4.249</b>	4.601
Average	RMSE	3.406	3.372	<b>3.042</b>	3.196
	SSIM	0.860	0.7845	<b>0.861</b>	0.800
	PSNR	<b>22.436</b>	21.371	22.279	21.736
	SAM	7.054	6.408	<b>5.96</b>	6.452
	CC	0.618	0.601	<b>0.643</b>	0.576
	ERGAS	4.754	4.5139	<b>4.068</b>	4.191

the predicted images by STTFN, EDCSTFN, and MLFF-GAN for the date 10-06-2023.

Based on the figure, the EDCSTFN algorithm demonstrates the best performance, effectively preserving spatial coherence and fine-grained details. It provides the smoothest and most visually accurate image compared to the other methods. No-

tably, EDCSTFN successfully predicted the LST around the Loire River, an area where the other algorithms struggled. In contrast, both STTFN and MLFF-GAN exhibit noticeable artifacts, with the edges of the patches clearly visible. These artifacts disrupt the spatial consistency and create visible boundaries in the fused images

## VI. LIMITATIONS AND FUTURE TRENDS

While DL-based STF methods have shown significant promise in enhancing LST estimation, our literature review and comparative study highlight several limitations and suggest future trends to address them. These insights aim to pave the way for more robust and effective applications of STF in LST modeling.

### A. Cloudy Conditions

The presence of clouds and their accompanying shadows pose a significant challenge to RS applications, as they obstruct the satellite's ability to capture clear and consistent images of the Earth's surface [237]. These obstructions result in missing or corrupted data [238]. In STF, researchers often address these gaps using interpolation techniques to estimate the missing values. However, the accuracy of these methods remains suboptimal, especially in regions with persistent cloud cover or highly dynamic land features. To overcome this limitation, a more effective approach would be to train DL models using datasets with missing pixels. This way, the network could learn to reconstruct gaps using the spatio-temporal relationships between the input datasets, such as  $X_1(s, t_1)$ ,  $P_1$ , or  $P_3$ . This would transform STF into a multi-objective problem, aiming not only to enhance spatial and temporal resolution but also to minimize the presence of missing pixels in the reconstructed images, as presented in Section III-A. As introduced in [70], the resulting STF model should generate outputs with either no missing pixels or a significantly reduced number of gaps. This study is one of the few that directly addresses the problem of cloud-induced gaps in STF.

### B. Inaccurate LST Estimations

LST is commonly estimated from satellite imagery using the algorithms presented in Section II-A. These algorithms inherently introduce errors, which can result in inaccurate LST estimations. In STF, multiple satellite images are fused, but when the input data already contains errors, these inaccuracies can propagate through the DL network. The initial errors in LST estimates are carried through the fusion process, potentially affecting the final predictions and leading to cumulative errors. For a more realistic and fair evaluation of STF methods, incorporating additional reliable data sources, such as ground-based sensors, would be valuable. Comparing STF outputs with these more accurate data would better assess the true performance of STF models while mitigating the influence of initial LST estimation errors [239], [240].

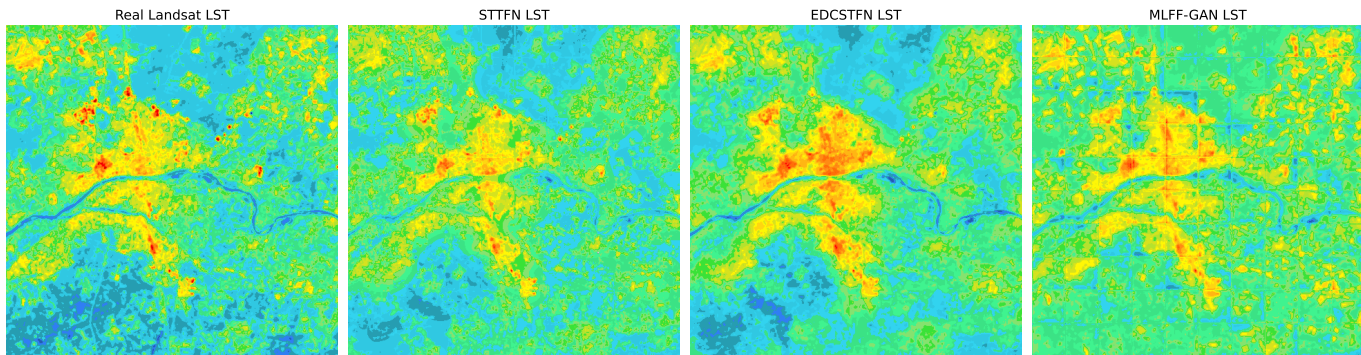


Fig. 19. Real image and predicted images for 10-06-2023, generated by STTFN, EDCSTFN, and MLFF-GAN.

### C. Transfer Learning

Transfer learning, although effective in various fields, remains underexplored in STF methods, with [63] being the only study to directly investigate its application in this domain. In general image fusion tasks, large-scale datasets such as ImageNet are often used to pre-train models for feature extraction. For instance, [241] and [242] employed ResNet50 to capture high-frequency features from source images, while [243] and [244] utilized VGG19 for feature extraction. Similarly, [245] applied DenseNet-201 pre-trained on ImageNet for deep feature extraction.

However, an alternative and potentially more effective approach would be to train the models directly on fusion-specific datasets, which enables them to learn unique features that are necessary for fusion tasks. Given the exponential growth of fusion images in the medical domain [246], established datasets could serve as a foundation for training models to handle fusion tasks, after which they can be fine-tuned for STF applications [247].

### D. Poor Generalibility

When transferring a trained model to a new region, one of the main challenges encountered is the domain shift problem. This arises because temporal dynamics, such as seasonal fluctuations, weather patterns, or urban development, can vary significantly between the region where the model was originally trained and the new region where it is being applied. These differences may hinder the model's ability to generalize effectively, as it may fail to account for the specific temporal characteristics of the new region. To overcome this challenge, fine-tuning the model becomes essential. Fine-tuning involves adapting the model to the new region's distinct temporal dynamics while preserving the generalization capabilities learned from the original data. A well-designed model for STF should be capable of generalizing across different regions by learning transferable features during training. For instance, studies like [83] assume that spatial relationships and sensor biases remain consistent from the original region to the transferred region, and thus propose that fine-tuning the model with a focus on temporal dynamics helps the model better address the unique characteristics of different regions.

### E. DL-Hybrid Methods

The current STF research lacks studies combining temporal DL models with spatial ones. While temporal networks, such as RNNs, have demonstrated effectiveness in capturing the temporal dynamics of satellite data, they often struggle with addressing spatial dependencies. In contrast, CNNs, GANs, AEs, and transformers excel at spatial feature extraction but are not typically designed for handling temporal data. Although the integration of CNNs with LSTMs has been investigated in a few studies, such as [72], hybrid DL models that combine both temporal and spatial architectures remain largely underexplored in STF.

### F. Insufficient spatial resolution

The DL-based STF methods are constrained by the spatial resolution of the lowest thermal satellite, Landsat, which provides a resolution of 30 meters. While this resolution is sufficient for many applications, it falls short in studies requiring higher precision, such as UHI analysis. UHIs demand a finer resolution to accurately capture temperature variations at the city scale. With a 30-meter resolution, details such as small urban features and microclimates are often missed.

To address this limitation, integrating satellites with higher spatial resolution, such as Sentinel-2, which provides 10-meter SR data, and PlanetScope, with a 3-meter resolution, can provide valuable information. While these satellites lack TIR sensors like those on Landsat or MODIS, their optical data can still be used in conjunction with thermal data from other sources to enhance spatial resolution. Studies have explored combining MODIS and Sentinel-2 [248] or Landsat-8 and Sentinel-2 [249] to estimate LST at 10 meters. However, these methods rely on traditional linear approaches, which are ineffective in providing accurate results.

### G. Integration of Large Language Models

Large Language Models (LLMs) have recently showcased remarkable abilities across various natural language processing tasks. Their success has spurred extensive research into expanding their applications. For instance, LLMs have been employed in domains like remote sensing data analysis [139], medical diagnosis [250], and computer programming [251].

This surge in LLM research prompts the question of whether they can be utilized in image fusion, specifically by extracting textual information from images and fusing this textual data alongside the visual content. In this approach, LLMs could integrate deeper semantic information beyond what is captured by visual features alone. For example, [252] demonstrated the generation of semantic prompts from images, which are then input into models like ChatGPT to produce comprehensive textual descriptions. These textual descriptions are subsequently fused within the textual domain, enhancing the fusion of visual information through cross-attention mechanisms. To date, this approach has not been applied within STF models. Integrating textual and visual data in STF could open an exciting new avenue for future research.

## VII. CONCLUSION

In this comprehensive survey, we have systematically analyzed and compared the latest advancements in STF methods, specifically those based on DL. We began by formulating the problem mathematically and introduced the DL techniques in this domain. Building on this foundation, we proposed a novel taxonomy, categorizing existing approaches across five key criteria: Architecture, Learning Algorithm, Training Strategy, and the Use of Pre-trained Models. Furthermore, we introduced a pioneering dataset, as to the best of our knowledge is the first publicly available and most recent MODIS-Landsat LST pairs dataset. Through extensive experiments conducted on this dataset, we evaluated the reliability and performance of various methods and we provided in-depth discussions on each outcome. To conclude, we highlighted the limitations of current approaches and outlined promising avenues for future research. We believe that our taxonomy, dataset, and empirical evaluations will not only enhance the understanding of DL-based STF methods but also pave the way for future innovations in this field.

## VIII. ACKNOWLEDGMENT

This work was carried out as a part of the CHOISIR project funded by Métropole d'Orléans, Région Centre-Val de Loire, and supported by 3ZA company.

## REFERENCES

- [1] P. R. Bureau, "2007 world population data sheet," *Population Reference*, 2007.
- [2] J. Vanos, S. Cakmak, L. Kalkstein, and A. Yagouti, "Association of weather and air pollution interactions on daily mortality in 12 canadian cities," *Air Quality, Atmosphere & Health*, vol. 8, pp. 307–320, 2015.
- [3] M. Nuruzzaman, "Urban heat island: causes, effects and mitigation measures—a review," *International Journal of Environmental Monitoring and Analysis*, vol. 3, no. 2, pp. 67–73, 2015.
- [4] M. Masiol, C. Agostinelli, G. Formenton, E. Tarabotti, and B. Pavoni, "Thirteen years of air pollution hourly monitoring in a large city: potential sources, trends, cycles and effects of car-free days," *Science of the Total Environment*, vol. 494, pp. 84–96, 2014.
- [5] G. C. Hulley, D. Ghent, F. M. Götsche, P. C. Guillevic, D. J. Mildrexler, and C. Coll, "3 - land surface temperature," in *Taking the Temperature of the Earth*, G. C. Hulley and D. Ghent, Eds. Elsevier, 2019, pp. 57–127. [Online]. Available: <https://www.sciencedirect.com/science/article/pii/B9780128144589000034>
- [6] M. King, *EOS Science Plan: The State of Science in the EOS Program*. National Aeronautics and Space Administration, 1999, available at: <https://books.google.fr/books?id=PS9RAAAAMAAJ>.
- [7] R. Hollmann, C. J. Merchant, R. Saunders, C. Downy, M. Buchwitz, A. Cazenave, E. Chuvieco, P. Defourny, G. de Leeuw, R. Forsberg *et al.*, "The esa climate change initiative: Satellite data records for essential climate variables," *Bulletin of the American Meteorological Society*, vol. 94, no. 10, pp. 1541–1552, 2013.
- [8] X. Li, W. Zhou, and Z. Ouyang, "Relationship between land surface temperature and spatial pattern of greenspace: What are the effects of spatial resolution?" *Landscape and Urban Planning*, vol. 114, pp. 1–8, 2013.
- [9] Y. H. Kerr, J. P. Lagouarde, F. Nerry, and C. Ottlé, "Land surface temperature retrieval techniques and applications: Case of the avhrr," in *Thermal remote sensing in land surface processing*. CRC Press, 2004, pp. 33–109.
- [10] P. Schneider and S. J. Hook, "Space observations of inland water bodies show rapid surface warming since 1985," *Geophysical Research Letters*, vol. 37, no. 22, 2010.
- [11] D. K. Hall, J. C. Comiso, N. E. DiGirolamo, C. A. Shuman, J. R. Key, and L. S. Koenig, "A satellite-derived climate-quality data record of the clear-sky surface temperature of the greenland ice sheet," *Journal of Climate*, vol. 25, no. 14, pp. 4785–4798, 2012.
- [12] I. Ibrahim, A. A. Samah, and R. Fauzi, "Land surface temperature and biophysical factors in urban planning," in *International conference on ecosystem, environment and sustainable development, Kuala Lumpur, Malaysia*, vol. 68. Citeseer, 2012, pp. 1792–1797.
- [13] M. Maimaitiyiming, A. Ghulam, T. Tiyyip, F. Pla, P. Latorre-Carmona, Ü. Halik, M. Sawut, and M. Caetano, "Effects of green space spatial pattern on land surface temperature: Implications for sustainable urban planning and climate change adaptation," *ISPRS Journal of Photogrammetry and Remote Sensing*, vol. 89, pp. 59–66, 2014.
- [14] S. Luysaert, M. Jammot, P. C. Stoy, S. Estel, J. Pongratz, E. Ceschia, G. Churkina, A. Don, K. Erb, M. Ferlicoq *et al.*, "Land management and land-cover change have impacts of similar magnitude on surface temperature," *Nature Climate Change*, vol. 4, no. 5, pp. 389–393, 2014.
- [15] A.-A. Kafy, M. S. Rahman, M. M. Hasan, M. Islam *et al.*, "Modelling future land use land cover changes and their impacts on land surface temperatures in rajshahi, bangladesh," *Remote Sensing Applications: Society and Environment*, vol. 18, p. 100314, 2020.
- [16] Z.-L. Li, B.-H. Tang, H. Wu, H. Ren, G. Yan, Z. Wan, I. F. Trigo, and J. A. Sobrino, "Satellite-derived land surface temperature: Current status and perspectives," *Remote sensing of environment*, vol. 131, pp. 14–37, 2013.
- [17] Z. Wan and J. Dozier, "A generalized split-window algorithm for retrieving land-surface temperature from space," *IEEE Transactions on geoscience and remote sensing*, vol. 34, no. 4, pp. 892–905, 1996.
- [18] A. Gillespie, S. Rokugawa, T. Matsunaga, J. S. Cothorn, S. Hook, and A. B. Kahle, "A temperature and emissivity separation algorithm for advanced spaceborne thermal emission and reflection radiometer (aster) images," *IEEE transactions on geoscience and remote sensing*, vol. 36, no. 4, pp. 1113–1126, 1998.
- [19] D. Sun and R. T. Pinker, "Estimation of land surface temperature from a geostationary operational environmental satellite (goes-8)," *Journal of geophysical research: atmospheres*, vol. 108, no. D11, 2003.
- [20] I. F. Trigo, C. C. Dacamara, P. Viterbo, J.-L. Roujean, F. Olesen, C. Barroso, F. Camacho-de Coca, D. Carrer, S. C. Freitas, J. García-Haro *et al.*, "The satellite application facility for land surface analysis," *International Journal of Remote Sensing*, vol. 32, no. 10, pp. 2725–2744, 2011.
- [21] N. K. Malakar, G. C. Hulley, S. J. Hook, K. Laraby, M. Cook, and J. R. Schott, "An operational land surface temperature product for landsat thermal data: Methodology and validation," *IEEE Transactions on Geoscience and Remote Sensing*, vol. 56, no. 10, pp. 5717–5735, 2018.
- [22] B. Koetz, W. Bastiaanssen, M. Berger, P. Defourny, U. Del Bello, M. Drusch, M. Drinkwater, R. Duca, V. Fernandez, D. Ghent *et al.*, "High spatio-temporal resolution land surface temperature mission—a copernicus candidate mission in support of agricultural monitoring," in *Igarss 2018-2018 IEEE international geoscience and remote sensing symposium*. IEEE, 2018, pp. 8160–8162.
- [23] Y. Shen, H. Shen, Q. Cheng, and L. Zhang, "Generating comparable and fine-scale time series of summer land surface temperature for thermal environment monitoring," *IEEE Journal of Selected Topics in Applied Earth Observations and Remote Sensing*, vol. 14, pp. 2136–2147, 2020.
- [24] B. Chen, B. Huang, and B. Xu, "Comparison of spatiotemporal fusion models: A review," *Remote Sensing*, vol. 7, no. 2, pp. 1798–1835, 2015.
- [25] H. Shen, X. Meng, and L. Zhang, "An integrated framework for the spatio-temporal-spectral fusion of remote sensing images," *IEEE*

- Transactions on Geoscience and Remote Sensing*, vol. 54, no. 12, pp. 7135–7148, 2016.
- [26] J. Zhang and J. Li, “Chapter 11 - spacecraft,” in *Spatial Cognitive Engine Technology*, J. Zhang and J. Li, Eds. Academic Press, 2023, pp. 129–162. [Online]. Available: <https://www.sciencedirect.com/science/article/pii/B9780323951074000044>
- [27] P. Gibson, “Chapter 1 - a systematic view of remote sensing (second edition),” in *Advanced Remote Sensing*, S. Liang and J. Wang, Eds. Academic Press, 2020, pp. 1–57. [Online]. Available: <https://www.sciencedirect.com/science/article/pii/B9780128158265000015>
- [28] W. Zhan, Y. Chen, J. Zhou, J. Wang, W. Liu, J. Voogt, X. Zhu, J. Quan, and J. Li, “Disaggregation of remotely sensed land surface temperature: Literature survey, taxonomy, issues, and caveats,” *Remote Sensing of Environment*, vol. 131, pp. 119–139, 2013.
- [29] Q. Mao, J. Peng, and Y. Wang, “Resolution enhancement of remotely sensed land surface temperature: Current status and perspectives,” *Remote Sensing*, vol. 13, no. 7, p. 1306, 2021.
- [30] M. Belgiu and A. Stein, “Spatiotemporal image fusion in remote sensing,” *Remote sensing*, vol. 11, no. 7, p. 818, 2019.
- [31] N. Agam, W. P. Kustas, M. C. Anderson, F. Li, and C. M. Neale, “A vegetation index based technique for spatial sharpening of thermal imagery,” *Remote sensing of Environment*, vol. 107, no. 4, pp. 545–558, 2007.
- [32] J. Nichol, “An emissivity modulation method for spatial enhancement of thermal satellite images in urban heat island analysis,” *Photogrammetric Engineering & Remote Sensing*, vol. 75, no. 5, pp. 547–556, 2009.
- [33] S.-B. Duan and Z.-L. Li, “Spatial downscaling of modis land surface temperatures using geographically weighted regression: Case study in northern china,” *IEEE Transactions on Geoscience and Remote Sensing*, vol. 54, no. 11, pp. 6458–6469, 2016.
- [34] Z. Xinming, S. Xiaoning, L. Pei, and H. Ronghai, “Spatial downscaling of land surface temperature with the multi-scale geographically weighted regression,” *National Remote Sensing Bulletin*, vol. 25, no. 8, pp. 1749–1766, 2021.
- [35] I. Agathangelidis and C. Cartalis, “Improving the disaggregation of modis land surface temperatures in an urban environment: A statistical downscaling approach using high-resolution emissivity,” *International Journal of Remote Sensing*, vol. 40, no. 13, pp. 5261–5286, 2019.
- [36] A. Dominguez, J. Kleissl, J. C. Luvall, and D. L. Rickman, “High-resolution urban thermal sharpener (huts),” *Remote Sensing of Environment*, vol. 115, no. 7, pp. 1772–1780, 2011.
- [37] W. Zhan, F. Huang, J. Quan, X. Zhu, L. Gao, J. Zhou, and W. Ju, “Disaggregation of remotely sensed land surface temperature: A new dynamic methodology,” *Journal of Geophysical Research: Atmospheres*, vol. 121, no. 18, pp. 10–538, 2016.
- [38] X. Zhu, F. Cai, J. Tian, and T. K.-A. Williams, “Spatiotemporal fusion of multisource remote sensing data: Literature survey, taxonomy, principles, applications, and future directions,” *Remote Sensing*, vol. 10, no. 4, p. 527, 2018.
- [39] H. Song, Q. Liu, G. Wang, R. Hang, and B. Huang, “Spatiotemporal satellite image fusion using deep convolutional neural networks,” *IEEE Journal of Selected Topics in Applied Earth Observations and Remote Sensing*, vol. 11, no. 3, pp. 821–829, 2018.
- [40] J. Kim and T. S. Hogue, “Evaluation and sensitivity testing of a coupled landsat-modis downscaling method for land surface temperature and vegetation indices in semi-arid regions,” *Journal of Applied Remote Sensing*, vol. 6, no. 1, pp. 063 569–063 569, 2012.
- [41] F. Gao, J. Masek, M. Schwaller, and F. Hall, “On the blending of the landsat and modis surface reflectance: Predicting daily landsat surface reflectance,” *IEEE Transactions on Geoscience and Remote Sensing*, vol. 44, no. 8, pp. 2207–2218, 2006.
- [42] X. Zhu, J. Chen, F. Gao, X. Chen, and J. G. Masek, “An enhanced spatial and temporal adaptive reflectance fusion model for complex heterogeneous regions,” *Remote Sensing of Environment*, vol. 114, no. 11, pp. 2610–2623, 2010.
- [43] P. Wu, H. Shen, T. Ai, and Y. Liu, “Land-surface temperature retrieval at high spatial and temporal resolutions based on multi-sensor fusion,” *International Journal of Digital Earth*, vol. 6, no. sup1, pp. 113–133, 2013.
- [44] B. Huang, J. Wang, H. Song, D. Fu, and K. Wong, “Generating high spatiotemporal resolution land surface temperature for urban heat island monitoring,” *IEEE Geoscience and Remote Sensing Letters*, vol. 10, no. 5, pp. 1011–1015, 2013.
- [45] P. Wu, H. Shen, L. Zhang, and F.-M. Göttsche, “Integrated fusion of multi-scale polar-orbiting and geostationary satellite observations for the mapping of high spatial and temporal resolution land surface temperature,” *Remote Sensing of Environment*, vol. 156, pp. 169–181, 2015.
- [46] M. Wu, Z. Niu, C. Wang, C. Wu, and L. Wang, “Use of modis and landsat time series data to generate high-resolution temporal synthetic landsat data using a spatial and temporal reflectance fusion model,” *Journal of Applied Remote Sensing*, vol. 6, no. 1, pp. 063 507–063 507, 2012.
- [47] W. Zhang, A. Li, H. Jin, J. Bian, Z. Zhang, G. Lei, Z. Qin, and C. Huang, “An enhanced spatial and temporal data fusion model for fusing landsat and modis surface reflectance to generate high temporal landsat-like data,” *Remote Sensing*, vol. 5, no. 10, pp. 5346–5368, 2013.
- [48] H. K. Zhang, B. Huang, M. Zhang, K. Cao, and L. Yu, “A generalization of spatial and temporal fusion methods for remotely sensed surface parameters,” *International Journal of Remote Sensing*, vol. 36, no. 17, pp. 4411–4445, 2015.
- [49] M. Wu, W. Huang, Z. Niu, and C. Wang, “Generating daily synthetic landsat imagery by combining landsat and modis data,” *Sensors*, vol. 15, no. 9, pp. 24 002–24 025, 2015.
- [50] X. Zhu, E. H. Helmer, F. Gao, D. Liu, J. Chen, and M. A. Lefsky, “A flexible spatiotemporal method for fusing satellite images with different resolutions,” *Remote Sensing of Environment*, vol. 172, pp. 165–177, 2016.
- [51] X. Li, F. Ling, G. M. Foody, Y. Ge, Y. Zhang, and Y. Du, “Generating a series of fine spatial and temporal resolution land cover maps by fusing coarse spatial resolution remotely sensed images and fine spatial resolution land cover maps,” *Remote Sensing of Environment*, vol. 196, pp. 293–311, 2017.
- [52] J. Quan, W. Zhan, T. Ma, Y. Du, Z. Guo, and B. Qin, “An integrated model for generating hourly landsat-like land surface temperatures over heterogeneous landscapes,” *Remote Sensing of Environment*, vol. 206, pp. 403–423, 2018.
- [53] H. Xia, Y. Chen, Y. Li, and J. Quan, “Combining kernel-driven and fusion-based methods to generate daily high-spatial-resolution land surface temperatures,” *Remote Sensing of Environment*, vol. 224, pp. 259–274, 2019.
- [54] B. Huang and H. Song, “Spatiotemporal reflectance fusion via sparse representation,” *IEEE Transactions on Geoscience and Remote Sensing*, vol. 50, no. 10, pp. 3707–3716, 2012.
- [55] B. Wu, B. Huang, and L. Zhang, “An error-bound-regularized sparse coding for spatiotemporal reflectance fusion,” *IEEE Transactions on Geoscience and Remote Sensing*, vol. 53, no. 12, pp. 6791–6803, 2015.
- [56] J. Wei, L. Wang, P. Liu, and W. Song, “Spatiotemporal fusion of remote sensing images with structural sparsity and semi-coupled dictionary learning,” *Remote Sensing*, vol. 9, no. 1, p. 21, 2016.
- [57] Y. Peng, W. Li, X. Luo, J. Du, X. Zhang, Y. Gan, and X. Gao, “Spatiotemporal reflectance fusion via tensor sparse representation,” *IEEE Transactions on Geoscience and Remote Sensing*, vol. 60, pp. 1–18, 2021.
- [58] A. Li, Y. Bo, Y. Zhu, P. Guo, J. Bi, and Y. He, “Blending multi-resolution satellite sea surface temperature (sst) products using bayesian maximum entropy method,” *Remote sensing of environment*, vol. 135, pp. 52–63, 2013.
- [59] B. Huang, H. Zhang, H. Song, J. Wang, and C. Song, “Unified fusion of remote-sensing imagery: Generating simultaneously high-resolution synthetic spatial–temporal–spectral earth observations,” *Remote sensing letters*, vol. 4, no. 6, pp. 561–569, 2013.
- [60] L. Liao, J. Song, J. Wang, Z. Xiao, and J. Wang, “Bayesian method for building frequent landsat-like ndvi datasets by integrating modis and landsat ndvi,” *Remote Sensing*, vol. 8, no. 6, p. 452, 2016.
- [61] J. Xue, Y. Leung, and T. Fung, “A bayesian data fusion approach to spatio-temporal fusion of remotely sensed images,” *Remote Sensing*, vol. 9, no. 12, p. 1310, 2017.
- [62] P. Adesso, M. Longo, R. Restaino, and G. Vivone, “Sequential bayesian methods for resolution enhancement of tir image sequences,” *IEEE Journal of Selected Topics in Applied Earth Observations and Remote Sensing*, vol. 8, no. 1, pp. 233–243, 2014.
- [63] Y. Chen, Y. Yang, X. Pan, X. Meng, and J. Hu, “Spatiotemporal fusion network for land surface temperature based on a conditional variational autoencoder,” *IEEE Transactions on Geoscience and Remote Sensing*, vol. 60, pp. 1–13, 2022.
- [64] Z. Tan, P. Yue, L. Di, and J. Tang, “Deriving high spatiotemporal remote sensing images using deep convolutional network,” *Remote Sensing*, vol. 10, no. 7, p. 1066, 2018.
- [65] X. Liu, C. Deng, J. Chanussot, D. Hong, and B. Zhao, “Stfnet: A two-stream convolutional neural network for spatiotemporal image fusion,” *IEEE Transactions on Geoscience and Remote Sensing*, vol. 57, no. 9, pp. 6552–6564, 2019.



- [66] Y. Zheng, H. Song, L. Sun, Z. Wu, and B. Jeon, "Spatiotemporal fusion of satellite images via very deep convolutional networks," *Remote Sensing*, vol. 11, no. 22, p. 2701, 2019.
- [67] Z. Yin, P. Wu, G. M. Foody, Y. Wu, Z. Liu, Y. Du, and F. Ling, "Spatiotemporal fusion of land surface temperature based on a convolutional neural network," *IEEE Transactions on Geoscience and Remote Sensing*, vol. 59, no. 2, pp. 1808–1822, 2020.
- [68] X. Wang and X. Wang, "Spatiotemporal fusion of remote sensing image based on deep learning," *Journal of Sensors*, vol. 2020, no. 1, p. 8873079, 2020.
- [69] Y. Li, J. Li, L. He, J. Chen, and A. Plaza, "A new sensor bias-driven spatio-temporal fusion model based on convolutional neural networks," *Science China Information Sciences*, vol. 63, pp. 1–16, 2020.
- [70] P. Qin, H. Huang, H. Tang, J. Wang, and C. Liu, "Mustfn: A spatiotemporal fusion method for multi-scale and multi-sensor remote sensing images based on a convolutional neural network," *International Journal of Applied Earth Observation and Geoinformation*, vol. 115, p. 103113, 2022.
- [71] W. Sun, J. Li, M. Jiang, and Q. Yuan, "Supervised and self-supervised learning-based cascade spatiotemporal fusion framework and its application," *ISPRS Journal of Photogrammetry and Remote Sensing*, vol. 203, pp. 19–36, 2023.
- [72] X. Meng, Q. Liu, F. Shao, and S. Li, "Spatio-temporal-spectral collaborative learning for spatio-temporal fusion with land cover changes," *IEEE Transactions on Geoscience and Remote Sensing*, vol. 60, pp. 1–16, 2022.
- [73] Z. Tan, L. Di, M. Zhang, L. Guo, and M. Gao, "An enhanced deep convolutional model for spatiotemporal image fusion," *Remote Sensing*, vol. 11, no. 24, p. 2898, 2019.
- [74] M. Jiang and H. Shao, "A cnn-transformer combined remote sensing imagery spatiotemporal fusion model," *IEEE Journal of Selected Topics in Applied Earth Observations and Remote Sensing*, 2024.
- [75] J. Chen, L. Wang, R. Feng, P. Liu, W. Han, and X. Chen, "Cyclegan-stf: Spatiotemporal fusion via cyclegan-based image generation," *IEEE Transactions on Geoscience and Remote Sensing*, vol. 59, no. 7, pp. 5851–5865, 2020.
- [76] H. Zhang, Y. Song, C. Han, and L. Zhang, "Remote sensing image spatiotemporal fusion using a generative adversarial network," *IEEE Transactions on Geoscience and Remote Sensing*, vol. 59, no. 5, pp. 4273–4286, 2020.
- [77] Y. Ma, J. Wei, W. Tang, and R. Tang, "Explicit and stepwise models for spatiotemporal fusion of remote sensing images with deep neural networks," *International Journal of Applied Earth Observation and Geoinformation*, vol. 105, p. 102611, 2021.
- [78] Z. Tan, M. Gao, X. Li, and L. Jiang, "A flexible reference-insensitive spatiotemporal fusion model for remote sensing images using conditional generative adversarial network," *IEEE Transactions on Geoscience and Remote Sensing*, vol. 60, pp. 1–13, 2021.
- [79] H. Zhang, Y. Sun, W. Shi, D. Guo, and N. Zheng, "An object-based spatiotemporal fusion model for remote sensing images," *European Journal of Remote Sensing*, vol. 54, no. 1, pp. 86–101, 2021.
- [80] B. Song, P. Liu, J. Li, L. Wang, L. Zhang, G. He, L. Chen, and J. Liu, "Mlff-gan: A multilevel feature fusion with gan for spatiotemporal remote sensing images," *IEEE Transactions on Geoscience and Remote Sensing*, vol. 60, pp. 1–16, 2022.
- [81] Z. Tan, M. Gao, J. Yuan, L. Jiang, and H. Duan, "A robust model for modis and landsat image fusion considering input noise," *IEEE Transactions on Geoscience and Remote Sensing*, vol. 60, pp. 1–17, 2022.
- [82] X. Pan, M. Deng, Z. Ao, and Q. Xin, "An adaptive multiscale generative adversarial network for the spatiotemporal fusion of landsat and modis data," *Remote Sensing*, vol. 15, no. 21, p. 5128, 2023.
- [83] H. Huang, W. He, H. Zhang, Y. Xia, and L. Zhang, "Stfdiff: Remote sensing image spatiotemporal fusion with diffusion models," *Information Fusion*, p. 102505, 2024.
- [84] W. Li, D. Cao, Y. Peng, and C. Yang, "Msnet: A multi-stream fusion network for remote sensing spatiotemporal fusion based on transformer and convolution," *Remote Sensing*, vol. 13, no. 18, p. 3724, 2021.
- [85] G. Yang, Y. Qian, H. Liu, B. Tang, R. Qi, Y. Lu, and J. Geng, "Msfusion: Multistage for remote sensing image spatiotemporal fusion based on texture transformer and convolutional neural network," *IEEE Journal of Selected Topics in Applied Earth Observations and Remote Sensing*, vol. 15, pp. 4653–4666, 2022.
- [86] G. Chen, P. Jiao, Q. Hu, L. Xiao, and Z. Ye, "Swinstfm: Remote sensing spatiotemporal fusion using swin transformer," *IEEE Transactions on Geoscience and Remote Sensing*, vol. 60, pp. 1–18, 2022.
- [87] W. Li, D. Cao, and M. Xiang, "Enhanced multi-stream remote sensing spatiotemporal fusion network based on transformer and dilated convolution," *Remote Sensing*, vol. 14, no. 18, p. 4544, 2022.
- [88] T. Benzenati, A. Kallel, and Y. Kessentini, "Stf-trans: A two-stream spatiotemporal fusion transformer for very high resolution satellites images," *Neurocomputing*, vol. 563, p. 126868, 2024.
- [89] Z. Yang, C. Diao, and B. Li, "A robust hybrid deep learning model for spatiotemporal image fusion," *Remote Sensing*, vol. 13, no. 24, p. 5005, 2021.
- [90] W. Zhan, F. Luo, H. Luo, J. Li, Y. Wu, Z. Yin, Y. Wu, and P. Wu, "Time-series-based spatiotemporal fusion network for improving crop type mapping," *Remote Sensing*, vol. 16, no. 2, p. 235, 2024.
- [91] P. Wu, Z. Yin, C. Zeng, S.-B. Duan, F.-M. Göttsche, X. Ma, X. Li, H. Yang, and H. Shen, "Spatially continuous and high-resolution land surface temperature product generation: A review of reconstruction and spatiotemporal fusion techniques," *IEEE Geoscience and Remote Sensing Magazine*, vol. 9, no. 3, pp. 112–137, 2021.
- [92] C. Yoo, J. Im, S. Park, and D. Cho, "Spatial downscaling of modis land surface temperature: Recent research trends, challenges, and future directions," *Korean Journal of Remote Sensing*, vol. 36, no. 4, pp. 609–626, 2020.
- [93] L. Ran, W. Mengmeng, Z. Zhengjia, H. Tian, and L. Xiuguo, "A review of spatiotemporal fusion methods for remotely sensed land surface temperature," *National Remote Sensing Bulletin*, vol. 26, no. 12, pp. 2433–2450, 2024.
- [94] J. Li, Y. Li, L. He, J. Chen, and A. Plaza, "Spatio-temporal fusion for remote sensing data: An overview and new benchmark," *Science China Information Sciences*, vol. 63, pp. 1–17, 2020.
- [95] A. Ferchichi, A. B. Abbes, V. Barra, and I. R. Farah, "Forecasting vegetation indices from spatio-temporal remotely sensed data using deep learning-based approaches: A systematic literature review," *Ecological Informatics*, vol. 68, p. 101552, 2022.
- [96] Z. Wang, Y. Ma, and Y. Zhang, "Review of pixel-level remote sensing image fusion based on deep learning," *Information Fusion*, vol. 90, pp. 36–58, 2023.
- [97] Q. Wang, Y. Tang, Y. Ge, H. Xie, X. Tong, and P. M. Atkinson, "A comprehensive review of spatial-temporal-spectral information reconstruction techniques," *Science of Remote Sensing*, p. 100102, 2023.
- [98] J. Xiao, A. K. Aggarwal, N. H. Duc, A. Arya, U. K. Rage, and R. Avtar, "A review of remote sensing image spatiotemporal fusion: Challenges, applications and recent trends," *Remote Sensing Applications: Society and Environment*, vol. 32, p. 101005, 2023.
- [99] G. Chen, H. Lu, W. Zou, L. Li, M. Emam, X. Chen, W. Jing, J. Wang, and C. Li, "Spatiotemporal fusion for spectral remote sensing: A statistical analysis and review," *Journal of King Saud University-Computer and Information Sciences*, vol. 35, no. 3, pp. 259–273, 2023.
- [100] J. Cui, J. Li, X. Gu, W. Zhang, D. Wang, X. Sun, Y. Zhan, J. Yang, Y. Liu, and X. Yang, "Comprehensive analysis of temporal-spatial fusion from 1991 to 2023 using bibliometric tools," *Atmosphere*, vol. 15, no. 5, p. 598, 2024.
- [101] S. Anand and R. Sharma, "Pansharpening and spatiotemporal image fusion method for remote sensing," *Engineering Research Express*, vol. 6, no. 2, p. 022201, 2024.
- [102] R. Swain, A. Paul, and M. D. Behera, "Spatio-temporal fusion methods for spectral remote sensing: a comprehensive technical review and comparative analysis," *Tropical Ecology*, vol. 65, no. 3, pp. 356–375, 2024.
- [103] J. M. Norman and F. Becker, "Terminology in thermal infrared remote sensing of natural surfaces," *Agricultural and Forest Meteorology*, vol. 77, no. 3-4, pp. 153–166, 1995.
- [104] A. Prata, V. Caselles, C. Coll, J. Sobrino, and C. Otlle, "Thermal remote sensing of land surface temperature from satellites: Current status and future prospects," *Remote sensing reviews*, vol. 12, no. 3-4, pp. 175–224, 1995.
- [105] P. Dash, F.-M. Göttsche, F.-S. Olesen, and H. Fischer, "Land surface temperature and emissivity estimation from passive sensor data: Theory and practice-current trends," *International Journal of remote sensing*, vol. 23, no. 13, pp. 2563–2594, 2002.
- [106] Z.-L. Li, H. Wu, S.-B. Duan, W. Zhao, H. Ren, X. Liu, P. Leng, R. Tang, X. Ye, J. Zhu *et al.*, "Satellite remote sensing of global land surface temperature: Definition, methods, products, and applications," *Reviews of Geophysics*, vol. 61, no. 1, 2023.
- [107] F. Becker and Z.-L. Li, "Surface temperature and emissivity at various scales: Definition, measurement and related problems," *Remote sensing reviews*, vol. 12, no. 3-4, pp. 225–253, 1995.
- [108] S.-B. Duan, Z.-L. Li, J. Cheng, and P. Leng, "Cross-satellite comparison of operational land surface temperature products derived from

- modis and aster data over bare soil surfaces,” *ISPRS Journal of Photogrammetry and Remote Sensing*, vol. 126, pp. 1–10, 2017.
- [109] J. C. Jimenez-Munoz, J. A. Sobrino, D. Skoković, C. Mattar, and J. Cristobal, “Land surface temperature retrieval methods from landsat-8 thermal infrared sensor data,” *IEEE Geoscience and remote sensing letters*, vol. 11, no. 10, pp. 1840–1843, 2014.
- [110] O. Rozenstein, Z. Qin, Y. Derimian, and A. Karnieli, “Derivation of land surface temperature for landsat-8 tirs using a split window algorithm,” *Sensors*, vol. 14, no. 4, pp. 5768–5780, 2014.
- [111] F. Wang, Z. Qin, C. Song, L. Tu, A. Karnieli, and S. Zhao, “An improved mono-window algorithm for land surface temperature retrieval from landsat 8 thermal infrared sensor data,” *Remote sensing*, vol. 7, no. 4, pp. 4268–4289, 2015.
- [112] D. X. Tran, F. Pla, P. Latorre-Carmona, S. W. Myint, M. Caetano, and H. V. Kieu, “Characterizing the relationship between land use land cover change and land surface temperature,” *ISPRS Journal of Photogrammetry and Remote Sensing*, vol. 124, pp. 119–132, 2017.
- [113] S. Wang, Y. Luo, X. Li, K. Yang, Q. Liu, X. Luo, and X. Li, “Down-scaling land surface temperature based on non-linear geographically weighted regressive model over urban areas,” *Remote Sensing*, vol. 13, no. 8, p. 1580, 2021.
- [114] Y. Tian, D. Su, S. Lauria, and X. Liu, “Recent advances on loss functions in deep learning for computer vision,” *Neurocomputing*, vol. 497, pp. 129–158, 2022.
- [115] O. Skean, A. Dhakal, N. Jacobs, and L. G. S. Giraldo, “Frossl: Frobenius norm minimization for self-supervised learning,” *arXiv preprint arXiv:2310.02903*, 2023.
- [116] Y. He, C. Zhu, J. Wang, M. Savvides, and X. Zhang, “Bounding box regression with uncertainty for accurate object detection,” in *Proceedings of the IEEE/CVF conference on computer vision and pattern recognition*, 2019, pp. 2888–2897.
- [117] P. J. Huber, “Robust estimation of a location parameter,” in *Breakthroughs in statistics: Methodology and distribution*. Springer, 1992, pp. 492–518.
- [118] S. Huang, L. Tang, J. P. Hupy, Y. Wang, and G. Shao, “A commentary review on the use of normalized difference vegetation index (ndvi) in the era of popular remote sensing,” *Journal of Forestry Research*, vol. 32, no. 1, pp. 1–6, 2021.
- [119] Y. Zha, J. Gao, and S. Ni, “Use of normalized difference built-up index in automatically mapping urban areas from tm imagery,” *International journal of remote sensing*, vol. 24, no. 3, pp. 583–594, 2003.
- [120] Z. Wang, A. C. Bovik, H. R. Sheikh, and E. P. Simoncelli, “Image quality assessment: from error visibility to structural similarity,” *IEEE transactions on image processing*, vol. 13, no. 4, pp. 600–612, 2004.
- [121] H. Zhao, O. Gallo, I. Frosio, and J. Kautz, “Loss functions for image restoration with neural networks,” *IEEE Transactions on computational imaging*, vol. 3, no. 1, pp. 47–57, 2016.
- [122] N. Khare, P. S. Thakur, P. Khanna, and A. Ojha, “Analysis of loss functions for image reconstruction using convolutional autoencoder,” in *International Conference on Computer Vision and Image Processing*. Springer, 2021, pp. 338–349.
- [123] B. Wu, H. Duan, Z. Liu, and G. Sun, “Srpgan: perceptual generative adversarial network for single image super resolution,” *arXiv preprint arXiv:1712.05927*, 2017.
- [124] I. Goodfellow, J. Pouget-Abadie, M. Mirza, B. Xu, D. Warde-Farley, S. Ozair, A. Courville, and Y. Bengio, “Generative adversarial nets,” *Advances in neural information processing systems*, vol. 27, 2014.
- [125] D. P. Kingma, “Adam: A method for stochastic optimization,” *arXiv preprint arXiv:1412.6980*, 2014.
- [126] J. Korhonen and J. You, “Peak signal-to-noise ratio revisited: Is simple beautiful?” in *2012 Fourth international workshop on quality of multimedia experience*. IEEE, 2012, pp. 37–38.
- [127] S. Kaneko, Y. Satoh, and S. Igarashi, “Using selective correlation coefficient for robust image registration,” *Pattern Recognition*, vol. 36, no. 5, pp. 1165–1173, 2003.
- [128] R. H. Yuhas, A. F. Goetz, and J. W. Boardman, “Discrimination among semi-arid landscape endmembers using the spectral angle mapper (sam) algorithm,” in *JPL, Summaries of the Third Annual JPL Airborne Geoscience Workshop. Volume 1: AVIRIS Workshop*, 1992.
- [129] Z. Wang and A. C. Bovik, “A universal image quality index,” *IEEE signal processing letters*, vol. 9, no. 3, pp. 81–84, 2002.
- [130] R. Zhang, P. Isola, A. A. Efros, E. Shechtman, and O. Wang, “The unreasonable effectiveness of deep features as a perceptual metric,” in *Proceedings of the IEEE conference on computer vision and pattern recognition*, 2018, pp. 586–595.
- [131] L. Alparone, S. Baronti, A. Garzelli, and F. Nencini, “A global quality measurement of pan-sharpened multispectral imagery,” *IEEE Geoscience and Remote Sensing Letters*, vol. 1, no. 4, pp. 313–317, 2004.
- [132] A. Krizhevsky, I. Sutskever, and G. E. Hinton, “Imagenet classification with deep convolutional neural networks,” *Advances in neural information processing systems*, vol. 25, 2012.
- [133] D.-X. Zhou, “Theory of deep convolutional neural networks: Down-sampling,” *Neural Networks*, vol. 124, pp. 319–327, 2020.
- [134] G. Li, M. Zhang, J. Li, F. Lv, and G. Tong, “Efficient densely connected convolutional neural networks,” *Pattern Recognition*, vol. 109, p. 107610, 2021.
- [135] Y. LeCun, Y. Bengio, and G. Hinton, “Deep learning,” *nature*, vol. 521, no. 7553, pp. 436–444, 2015.
- [136] J. Gu, Z. Wang, J. Kuen, L. Ma, A. Shahroudy, B. Shuai, T. Liu, X. Wang, G. Wang, J. Cai *et al.*, “Recent advances in convolutional neural networks,” *Pattern recognition*, vol. 77, pp. 354–377, 2018.
- [137] L. Alzubaidi, J. Zhang, A. J. Humaidi, A. Al-Dujaili, Y. Duan, O. Al-Shamma, J. Santamaría, M. A. Fadhel, M. Al-Amidie, and L. Farhan, “Review of deep learning: concepts, cnn architectures, challenges, applications, future directions,” *Journal of big Data*, vol. 8, pp. 1–74, 2021.
- [138] V. Nair and G. E. Hinton, “Rectified linear units improve restricted boltzmann machines,” in *Proceedings of the 27th international conference on machine learning (ICML-10)*, 2010, pp. 807–814.
- [139] X. Li, C. Wen, Y. Hu, Z. Yuan, and X. X. Zhu, “Vision-language models in remote sensing: Current progress and future trends,” *IEEE Geoscience and Remote Sensing Magazine*, 2024.
- [140] Y. LeCun, L. Bottou, Y. Bengio, and P. Haffner, “Gradient-based learning applied to document recognition,” *Proceedings of the IEEE*, vol. 86, no. 11, pp. 2278–2324, 1998.
- [141] J. Deng, W. Dong, R. Socher, L.-J. Li, K. Li, and L. Fei-Fei, “Imagenet: A large-scale hierarchical image database,” in *2009 IEEE conference on computer vision and pattern recognition*. Ieee, 2009, pp. 248–255.
- [142] K. Simonyan, “Very deep convolutional networks for large-scale image recognition,” *arXiv preprint arXiv:1409.1556*, 2014.
- [143] C. Szegedy, W. Liu, Y. Jia, P. Sermanet, S. Reed, D. Anguelov, D. Erhan, V. Vanhoucke, and A. Rabinovich, “Going deeper with convolutions,” in *Proceedings of the IEEE conference on computer vision and pattern recognition*, 2015, pp. 1–9.
- [144] K. He, X. Zhang, S. Ren, and J. Sun, “Deep residual learning for image recognition,” in *Proceedings of the IEEE conference on computer vision and pattern recognition*, 2016, pp. 770–778.
- [145] G. Huang, Z. Liu, L. Van Der Maaten, and K. Q. Weinberger, “Densely connected convolutional networks,” in *Proceedings of the IEEE conference on computer vision and pattern recognition*, 2017, pp. 4700–4708.
- [146] S. Xie, R. Girshick, P. Dollár, Z. Tu, and K. He, “Aggregated residual transformations for deep neural networks,” in *Proceedings of the IEEE conference on computer vision and pattern recognition*, 2017, pp. 1492–1500.
- [147] M. Tan and Q. Le, “Efficientnet: Rethinking model scaling for convolutional neural networks,” in *International conference on machine learning*. PMLR, 2019, pp. 6105–6114.
- [148] I. V. Emelyanova, T. R. McVicar, T. G. Van Niel, L. T. Li, and A. I. Van Dijk, “Assessing the accuracy of blending landsat–modis surface reflectances in two landscapes with contrasting spatial and temporal dynamics: A framework for algorithm selection,” *Remote Sensing of Environment*, vol. 133, pp. 193–209, 2013.
- [149] S. Yu, Y. Deng, Y. Li, J. Li, J. Chen, and S. Zhang, “An unsupervised model based on convolutional neural network for fusing landsat-8 and sentinel-2 data,” in *IGARSS 2024-2024 IEEE International Geoscience and Remote Sensing Symposium*. IEEE, 2024, pp. 9214–9217.
- [150] D. E. Rumelhart, G. E. Hinton, and R. J. Williams, “Learning internal representations by error propagation, parallel distributed processing, and the microstructure of cognition, ed. de rumelhart and j. mclelland. vol. 1. 1986,” *Biometrika*, vol. 71, no. 599-607, p. 6, 1986.
- [151] S. Chen and W. Guo, “Auto-encoders in deep learning—a review with new perspectives,” *Mathematics*, vol. 11, no. 8, p. 1777, 2023.
- [152] D. Bank, N. Koenigstein, and R. Giryes, “Machine learning for data science handbook: Data mining and knowledge discovery handbook,” 2023.
- [153] K. Berahmand, F. Daneshfar, E. S. Salehi, Y. Li, and Y. Xu, “Autoencoders and their applications in machine learning: a survey,” *Artificial Intelligence Review*, vol. 57, no. 2, p. 28, 2024.

- [154] Z. Yang, B. Xu, W. Luo, and F. Chen, "Autoencoder-based representation learning and its application in intelligent fault diagnosis: A review," *Measurement*, vol. 189, p. 110460, 2022.
- [155] D. Yu and M. L. Seltzer, "Improved bottleneck features using pre-trained deep neural networks," in *Twelfth annual conference of the international speech communication association*, 2011.
- [156] Z. Chai, W. Song, H. Wang, and F. Liu, "A semi-supervised auto-encoder using label and sparse regularizations for classification," *Applied Soft Computing*, vol. 77, pp. 205–217, 2019.
- [157] G. E. Hinton, S. Osindero, and Y.-W. Teh, "A fast learning algorithm for deep belief nets," *Neural computation*, vol. 18, no. 7, pp. 1527–1554, 2006.
- [158] D.-T. Hoang and H.-J. Kang, "A survey on deep learning based bearing fault diagnosis," *Neurocomputing*, vol. 335, pp. 327–335, 2019.
- [159] A. Ng *et al.*, "Sparse autoencoder," *CS294A Lecture notes*, vol. 72, no. 2011, pp. 1–19, 2011.
- [160] S. Rifai, P. Vincent, X. Muller, X. Glorot, and Y. Bengio, "Contractive auto-encoders: Explicit invariance during feature extraction," in *Proceedings of the 28th international conference on international conference on machine learning*, 2011, pp. 833–840.
- [161] P. Vincent, H. Larochelle, I. Lajoie, Y. Bengio, P.-A. Manzagol, and L. Bottou, "Stacked denoising autoencoders: Learning useful representations in a deep network with a local denoising criterion," *Journal of machine learning research*, vol. 11, no. 12, 2010.
- [162] F. Li, J. Zuradsky, and W. Wu, "Sparse representation learning of data by autoencoders with  $l^1$  sub  $1/2$  regularization," *Neural Network World*, vol. 28, no. 2, pp. 133–147, 2018.
- [163] J. An and S. Cho, "Variational autoencoder based anomaly detection using reconstruction probability," *Special lecture on IE*, vol. 2, no. 1, pp. 1–18, 2015.
- [164] A. Makhzani, J. Shlens, N. Jaitly, I. Goodfellow, and B. Frey, "Adversarial autoencoders," *arXiv preprint arXiv:1511.05644*, 2015.
- [165] S. Semeniuta, A. Severyn, and E. Barth, "A hybrid convolutional variational autoencoder for text generation," *arXiv preprint arXiv:1702.02390*, 2017.
- [166] H. D. Nguyen, K. P. Tran, S. Thomassey, and M. Hamad, "Forecasting and anomaly detection approaches using lstm and lstm autoencoder techniques with the applications in supply chain management," *International Journal of Information Management*, vol. 57, p. 102282, 2021.
- [167] A. Dehghan, E. G. Ortiz, R. Villegas, and M. Shah, "Who do i look like? determining parent-offspring resemblance via gated autoencoders," in *Proceedings of the IEEE conference on computer vision and pattern recognition*, 2014, pp. 1757–1764.
- [168] W. Xu, H. Sun, C. Deng, and Y. Tan, "Variational autoencoder for semi-supervised text classification," in *Proceedings of the AAAI conference on artificial intelligence*, vol. 31, no. 1, 2017.
- [169] I. Higgins, L. Matthey, A. Pal, C. P. Burgess, X. Glorot, M. M. Botvinick, S. Mohamed, and A. Lerchner, "beta-vae: Learning basic visual concepts with a constrained variational framework," *ICLR (Poster)*, vol. 3, 2017.
- [170] Z. Hou, X. Liu, Y. Cen, Y. Dong, H. Yang, C. Wang, and J. Tang, "Graphmae: Self-supervised masked graph autoencoders," in *Proceedings of the 28th ACM SIGKDD Conference on Knowledge Discovery and Data Mining*, 2022, pp. 594–604.
- [171] Z. Huang, X. Jin, C. Lu, Q. Hou, M.-M. Cheng, D. Fu, X. Shen, and J. Feng, "Contrastive masked autoencoders are stronger vision learners," *IEEE Transactions on Pattern Analysis and Machine Intelligence*, 2023.
- [172] P. Sharma, M. Kumar, H. K. Sharma, and S. M. Biju, "Generative adversarial networks (gans): Introduction, taxonomy, variants, limitations, and applications," *Multimedia Tools and Applications*, pp. 1–48, 2024.
- [173] Y. Hong, U. Hwang, J. Yoo, and S. Yoon, "How generative adversarial networks and their variants work: An overview," *ACM Computing Surveys (CSUR)*, vol. 52, no. 1, pp. 1–43, 2019.
- [174] I. Goodfellow, J. Pouget-Abadie, M. Mirza, B. Xu, D. Warde-Farley, S. Ozair, A. Courville, and Y. Bengio, "Generative adversarial networks," *Communications of the ACM*, vol. 63, no. 11, pp. 139–144, 2020.
- [175] J.-Y. Zhu, P. Krähenbühl, E. Shechtman, and A. A. Efros, "Generative visual manipulation on the natural image manifold," in *Computer Vision—ECCV 2016: 14th European Conference, Amsterdam, The Netherlands, October 11–14, 2016, Proceedings, Part V 14*. Springer, 2016, pp. 597–613.
- [176] C. Ledig, L. Theis, F. Huszár, J. Caballero, A. Cunningham, A. Acosta, A. Aitken, A. Tejani, J. Totz, Z. Wang *et al.*, "Photo-realistic single image super-resolution using a generative adversarial network," in *Proceedings of the IEEE conference on computer vision and pattern recognition*, 2017, pp. 4681–4690.
- [177] H. Zhang, V. Sindagi, and V. M. Patel, "Image de-raining using a conditional generative adversarial network," *IEEE transactions on circuits and systems for video technology*, vol. 30, no. 11, pp. 3943–3956, 2019.
- [178] J.-Y. Zhu, T. Park, P. Isola, and A. A. Efros, "Unpaired image-to-image translation using cycle-consistent adversarial networks," in *Proceedings of the IEEE international conference on computer vision*, 2017, pp. 2223–2232.
- [179] H. Lin, Y. Liu, S. Li, and X. Qu, "How generative adversarial networks promote the development of intelligent transportation systems: A survey," *IEEE/CAA journal of automatica sinica*, 2023.
- [180] E. L. Denton, S. Chintala, R. Fergus *et al.*, "Deep generative image models using a laplacian pyramid of adversarial networks," *Advances in neural information processing systems*, vol. 28, 2015.
- [181] A. Radford, "Unsupervised representation learning with deep convolutional generative adversarial networks," *arXiv preprint arXiv:1511.06434*, 2015.
- [182] X. Chen, Y. Duan, R. Houthoofd, J. Schulman, I. Sutskever, and P. Abbeel, "Infogan: Interpretable representation learning by information maximizing generative adversarial nets," *Advances in neural information processing systems*, vol. 29, 2016.
- [183] M. Mirza, "Conditional generative adversarial nets," *arXiv preprint arXiv:1411.1784*, 2014.
- [184] V. Dumoulin, I. Belghazi, B. Poole, O. Mastropietro, A. Lamb, M. Arjovsky, and A. Courville, "Adversarially learned inference," *arXiv preprint arXiv:1606.00704*, 2016.
- [185] J. Donahue, P. Krähenbühl, and T. Darrell, "Adversarial feature learning," *arXiv preprint arXiv:1605.09782*, 2016.
- [186] D. P. Kingma, "Auto-encoding variational bayes," *arXiv preprint arXiv:1312.6114*, 2013.
- [187] L. Mescheder, S. Nowozin, and A. Geiger, "Adversarial variational bayes: Unifying variational autoencoders and generative adversarial networks," in *International conference on machine learning*. PMLR, 2017, pp. 2391–2400.
- [188] Y. Xia, W. He, Q. Huang, H. Chen, H. Huang, and H. Zhang, "Sossf: Landsat-8 image synthesis on the blending of sentinel-1 and modis data," *IEEE Transactions on Geoscience and Remote Sensing*, 2024.
- [189] A. Vaswani, "Attention is all you need," *Advances in Neural Information Processing Systems*, 2017.
- [190] T. Wolf, L. Debut, V. Sanh, J. Chaumond, C. Delangue, A. Moi, P. Cistac, T. Rault, R. Louf, M. Funtowicz *et al.*, "Transformers: State-of-the-art natural language processing," in *Proceedings of the 2020 conference on empirical methods in natural language processing: system demonstrations*, 2020, pp. 38–45.
- [191] A. Dosovitskiy, "An image is worth 16x16 words: Transformers for image recognition at scale," *arXiv preprint arXiv:2010.11929*, 2020.
- [192] R. Azad, A. Kazerouni, M. Heidari, E. K. Aghdam, A. Molaei, Y. Jia, A. Jose, R. Roy, and D. Merhof, "Advances in medical image analysis with vision transformers: a comprehensive review," *Medical Image Analysis*, vol. 91, p. 103000, 2024.
- [193] C. Sun, A. Shrivastava, S. Singh, and A. Gupta, "Revisiting unreasonable effectiveness of data in deep learning era," in *Proceedings of the IEEE international conference on computer vision*, 2017, pp. 843–852.
- [194] A. Kolesnikov, L. Beyer, X. Zhai, J. Puigcerver, J. Yung, S. Gelly, and N. Houlsby, "Big transfer (bit): General visual representation learning," in *Computer Vision—ECCV 2020: 16th European Conference, Glasgow, UK, August 23–28, 2020, Proceedings, Part V 16*. Springer, 2020, pp. 491–507.
- [195] H. Touvron, M. Cord, M. Douze, F. Massa, A. Sablayrolles, and H. Jégou, "Training data-efficient image transformers & distillation through attention," in *International conference on machine learning*. PMLR, 2021, pp. 10347–10357.
- [196] K. Han, A. Xiao, E. Wu, J. Guo, C. Xu, and Y. Wang, "Transformer in transformer," *Advances in neural information processing systems*, vol. 34, pp. 15908–15919, 2021.
- [197] W. Wang, E. Xie, X. Li, D.-P. Fan, K. Song, D. Liang, T. Lu, P. Luo, and L. Shao, "Pyramid vision transformer: A versatile backbone for dense prediction without convolutions," in *Proceedings of the IEEE/CVF international conference on computer vision*, 2021, pp. 568–578.
- [198] Z. Liu, Y. Lin, Y. Cao, H. Hu, Y. Wei, Z. Zhang, S. Lin, and B. Guo, "Swin transformer: Hierarchical vision transformer using shifted windows," in *Proceedings of the IEEE/CVF international conference on computer vision*, 2021, pp. 10012–10022.

- [199] X. Chu, Z. Tian, Y. Wang, B. Zhang, H. Ren, X. Wei, H. Xia, and C. Shen, "Twins: Revisiting the design of spatial attention in vision transformers," *Advances in neural information processing systems*, vol. 34, pp. 9355–9366, 2021.
- [200] P. Zhang, X. Dai, J. Yang, B. Xiao, L. Yuan, L. Zhang, and J. Gao, "Multi-scale vision longformer: A new vision transformer for high-resolution image encoding," in *Proceedings of the IEEE/CVF international conference on computer vision*, 2021, pp. 2998–3008.
- [201] L. Yuan, Q. Hou, Z. Jiang, J. Feng, and S. Yan, "Volo: Vision outlooker for visual recognition," *IEEE transactions on pattern analysis and machine intelligence*, vol. 45, no. 5, pp. 6575–6586, 2022.
- [202] L. R. Medsker, L. Jain *et al.*, "Recurrent neural networks," *Design and Applications*, vol. 5, no. 64-67, p. 2, 2001.
- [203] S. Das, A. Tariq, T. Santos, S. S. Kantareddy, and I. Banerjee, "Recurrent neural networks (rnns): architectures, training tricks, and introduction to influential research," *Machine Learning for Brain Disorders*, pp. 117–138, 2023.
- [204] I. D. Mienye and N. Jere, "Deep learning for credit card fraud detection: A review of algorithms, challenges, and solutions," *IEEE Access*, 2024.
- [205] I. D. Mienye and Y. Sun, "A machine learning method with hybrid feature selection for improved credit card fraud detection," *Applied Sciences*, vol. 13, no. 12, p. 7254, 2023.
- [206] S. Hochreiter, "Long short-term memory," *Neural Computation MIT-Press*, 1997.
- [207] A. Graves and J. Schmidhuber, "Framewise phoneme classification with bidirectional lstm and other neural network architectures," *Neural networks*, vol. 18, no. 5-6, pp. 602–610, 2005.
- [208] Z. Karevan and J. A. Suykens, "Spatio-temporal stacked lstm for temperature prediction in weather forecasting," *arXiv preprint arXiv:1811.06341*, 2018.
- [209] K. Cho, "Learning phrase representations using rnn encoder-decoder for statistical machine translation," *arXiv preprint arXiv:1406.1078*, 2014.
- [210] F. A. Gers and J. Schmidhuber, "Recurrent nets that time and count," in *Proceedings of the IEEE-INNS-ENNS International Joint Conference on Neural Networks. IJCNN 2000. Neural Computing: New Challenges and Perspectives for the New Millennium*, vol. 3. IEEE, 2000, pp. 189–194.
- [211] H. Jaeger, "Adaptive nonlinear system identification with echo state networks," *Advances in neural information processing systems*, vol. 15, 2002.
- [212] S. Li, W. Li, C. Cook, C. Zhu, and Y. Gao, "Independently recurrent neural network (indrnn): Building a longer and deeper rnn," in *Proceedings of the IEEE conference on computer vision and pattern recognition*, 2018, pp. 5457–5466.
- [213] V. Rani, S. T. Nabi, M. Kumar, A. Mittal, and K. Kumar, "Self-supervised learning: A succinct review," *Archives of Computational Methods in Engineering*, vol. 30, no. 4, pp. 2761–2775, 2023.
- [214] M. Laal and S. M. Ghodsi, "Benefits of collaborative learning," *Procedia-social and behavioral sciences*, vol. 31, pp. 486–490, 2012.
- [215] M. Shafiq and Z. Gu, "Deep residual learning for image recognition: A survey," *Applied Sciences*, vol. 12, no. 18, p. 8972, 2022.
- [216] S. Wu, S. Zhong, and Y. Liu, "Deep residual learning for image steganalysis," *Multimedia tools and applications*, vol. 77, pp. 10437–10453, 2018.
- [217] D. Jia, C. Cheng, S. Shen, and L. Ning, "Multitask deep learning framework for spatiotemporal fusion of ndvi," *IEEE Transactions on Geoscience and Remote Sensing*, vol. 60, pp. 1–13, 2022.
- [218] L. Huang, J. Qin, Y. Zhou, F. Zhu, L. Liu, and L. Shao, "Normalization techniques in training dnns: Methodology, analysis and application," *IEEE transactions on pattern analysis and machine intelligence*, vol. 45, no. 8, pp. 10173–10196, 2023.
- [219] S. Ioffe, "Batch normalization: Accelerating deep network training by reducing internal covariate shift," *arXiv preprint arXiv:1502.03167*, 2015.
- [220] Y. Wu and K. He, "Group normalization," in *Proceedings of the European conference on computer vision (ECCV)*, 2018, pp. 3–19.
- [221] D. Ulyanov, "Instance normalization: The missing ingredient for fast stylization," *arXiv preprint arXiv:1607.08022*, 2016.
- [222] T. Miyato, T. Kataoka, M. Koyama, and Y. Yoshida, "Spectral normalization for generative adversarial networks," *arXiv preprint arXiv:1802.05957*, 2018.
- [223] P. Luo, J. Ren, Z. Peng, R. Zhang, and J. Li, "Differentiable learning-to-normalize via switchable normalization," *arXiv preprint arXiv:1806.10779*, 2018.
- [224] I. Salehin and D.-K. Kang, "A review on dropout regularization approaches for deep neural networks within the scholarly domain," *Electronics*, vol. 12, no. 14, p. 3106, 2023.
- [225] X. Ying, "An overview of overfitting and its solutions," in *Journal of physics: Conference series*, vol. 1168. IOP Publishing, 2019, p. 022022.
- [226] H. Chen, Y. Wang, T. Guo, C. Xu, Y. Deng, Z. Liu, S. Ma, C. Xu, C. Xu, and W. Gao, "Pre-trained image processing transformer," in *Proceedings of the IEEE/CVF conference on computer vision and pattern recognition*, 2021, pp. 12299–12310.
- [227] X. Qiu, T. Sun, Y. Xu, Y. Shao, N. Dai, and X. Huang, "Pre-trained models for natural language processing: A survey," *Science China technological sciences*, vol. 63, no. 10, pp. 1872–1897, 2020.
- [228] D. Erhan, A. Courville, Y. Bengio, and P. Vincent, "Why does unsupervised pre-training help deep learning?" in *Proceedings of the thirteenth international conference on artificial intelligence and statistics. JMLR Workshop and Conference Proceedings*, 2010, pp. 201–208.
- [229] E. d. S. Puls, M. V. Todescato, and J. L. Carbonera, "An evaluation of pre-trained models for feature extraction in image classification," *arXiv preprint arXiv:2310.02037*, 2023.
- [230] K. Weiss, T. M. Khoshgoftaar, and D. Wang, "A survey of transfer learning," *Journal of Big data*, vol. 3, pp. 1–40, 2016.
- [231] S. J. Pan and Q. Yang, "A survey on transfer learning," *IEEE Transactions on knowledge and data engineering*, vol. 22, no. 10, pp. 1345–1359, 2009.
- [232] N. Gorelick, M. Hancher, M. Dixon, S. Ilyushchenko, D. Thau, and R. Moore, "Google earth engine: Planetary-scale geospatial analysis for everyone," *Remote sensing of Environment*, vol. 202, pp. 18–27, 2017.
- [233] Z. Wan, "Modis land-surface temperature algorithm theoretical basis document (1st abtd)," *Institute for Computational Earth System Science, Santa Barbara*, vol. 75, p. 18, 1999.
- [234] S. L. Ermida, P. Soares, V. Mantas, F.-M. Göttsche, and I. F. Trigo, "Google earth engine open-source code for land surface temperature estimation from the landsat series," *Remote Sensing*, vol. 12, no. 9, p. 1471, 2020.
- [235] S.-B. Duan, Z.-L. Li, H. Wu, P. Leng, M. Gao, and C. Wang, "Radiance-based validation of land surface temperature products derived from collection 6 modis thermal infrared data," *International journal of applied earth observation and geoinformation*, vol. 70, pp. 84–92, 2018.
- [236] S.-B. Duan, Z.-L. Li, H. Li, F.-M. Göttsche, H. Wu, W. Zhao, P. Leng, X. Zhang, and C. Coll, "Validation of collection 6 modis land surface temperature product using in situ measurements," *Remote sensing of environment*, vol. 225, pp. 16–29, 2019.
- [237] Z. Li, H. Shen, Q. Cheng, Y. Liu, S. You, and Z. He, "Deep learning based cloud detection for medium and high resolution remote sensing images of different sensors," *ISPRS Journal of Photogrammetry and Remote Sensing*, vol. 150, pp. 197–212, 2019.
- [238] Y. Mo, Y. Xu, H. Chen, and S. Zhu, "A review of reconstructing remotely sensed land surface temperature under cloudy conditions," *Remote Sensing*, vol. 13, no. 14, p. 2838, 2021.
- [239] P. Krishnan, T. P. Meyers, S. J. Hook, M. Heuer, D. Senn, and E. J. Dumas, "Intercomparison of in situ sensors for ground-based land surface temperature measurements," *Sensors*, vol. 20, no. 18, p. 5268, 2020.
- [240] V. Shandas, Y. Makido, and A. N. Upraity, "Evaluating differences between ground-based and satellite-derived measurements of urban heat: The role of land cover classes in portland, oregon and washington, dc," *Land*, vol. 12, no. 3, p. 562, 2023.
- [241] H. Li, X.-j. Wu, and T. S. Durrani, "Infrared and visible image fusion with resnet and zero-phase component analysis," *Infrared Physics & Technology*, vol. 102, p. 103039, 2019.
- [242] D. Zhang, K. Ren, J. Zhou, G. Gu, and Q. Chen, "An infrared and visible image fusion method based on deep learning," in *4th Optics Young Scientist Summit (OYSS 2020)*, vol. 11781. SPIE, 2021, pp. 64–70.
- [243] H. Li, X.-J. Wu, and J. Kittler, "Infrared and visible image fusion using a deep learning framework," in *2018 24th international conference on pattern recognition (ICPR)*. IEEE, 2018, pp. 2705–2710.
- [244] X. Ren, F. Meng, T. Hu, Z. Liu, and C. Wang, "Infrared-visible image fusion based on convolutional neural networks (cnn)," in *Intelligence Science and Big Data Engineering: 8th International Conference, IScIDE 2018, Lanzhou, China, August 18–19, 2018, Revised Selected Papers 8*. Springer, 2018, pp. 301–307.

- [245] Y. Feng, H. Lu, J. Bai, L. Cao, and H. Yin, "Fully convolutional network-based infrared and visible image fusion," *Multimedia Tools and Applications*, vol. 79, no. 21, pp. 15 001–15 014, 2020.
- [246] Y. Li, J. Zhao, Z. Lv, and J. Li, "Medical image fusion method by deep learning," *International Journal of Cognitive Computing in Engineering*, vol. 2, pp. 21–29, 2021.
- [247] M. A. Azam, K. B. Khan, S. Salahuddin, E. Rehman, S. A. Khan, M. A. Khan, S. Kadry, and A. H. Gandomi, "A review on multimodal medical image fusion: Compendious analysis of medical modalities, multimodal databases, fusion techniques and quality metrics," *Computers in biology and medicine*, vol. 144, p. 105253, 2022.
- [248] J. M. Sánchez, J. M. Galve, J. González-Piqueras, R. López-Urrea, R. Niclòs, and A. Calera, "Monitoring 10-m lst from the combination modis/sentinel-2, validation in a high contrast semi-arid agroecosystem," *Remote Sensing*, vol. 12, no. 9, p. 1453, 2020.
- [249] Y. Abunnasr and M. Mhawej, "Towards a combined landsat-8 and sentinel-2 for 10-m land surface temperature products: The google earth engine monthly ten-st-gee system," *Environmental Modelling & Software*, vol. 155, p. 105456, 2022.
- [250] A. J. Thirunavukarasu, D. S. J. Ting, K. Elangovan, L. Gutierrez, T. F. Tan, and D. S. W. Ting, "Large language models in medicine," *Nature medicine*, vol. 29, no. 8, pp. 1930–1940, 2023.
- [251] F. F. Xu, U. Alon, G. Neubig, and V. J. Hellendoorn, "A systematic evaluation of large language models of code," in *Proceedings of the 6th ACM SIGPLAN International Symposium on Machine Programming*, 2022, pp. 1–10.
- [252] Z. Zhao, L. Deng, H. Bai, Y. Cui, Z. Zhang, Y. Zhang, H. Qin, D. Chen, J. Zhang, P. Wang *et al.*, "Image fusion via vision-language model," *arXiv preprint arXiv:2402.02235*, 2024.



**Sofiane Bouaziz** is PhD Student at INSA Centre Val de Loire (INSA CVL) and the PRISME Laboratory. He received his Master's and Engineering degrees in Computer Science and Artificial Intelligence from École Nationale Supérieure d'Informatique, Algiers, Algeria in 2023. His current research focuses on using Artificial Intelligence and Computer Vision to tackle challenges in remote sensing.



**Adel Hafiane** received the M.S. degree in embedded systems and information processing, and the Ph.D. degree from the University of Paris-Saclay, in 2002 and 2005, respectively. After that, he embarked on teaching and research, spending a year at Paris-Saclay and subsequently another year at INSA Centre Val de Loire (INSA CVL). He was postdoctoral fellow at the computer science department, University of Missouri, from 2007 to 2008. Since September 2008, as an assistant professor, then as an associate professor. He is a head of the Image and Vision group at PRISME Laboratory of University of Orléans and INSA CVL. He was an invited researcher at the University of Missouri on multiple periods, from 2009 to 2013. His research interests include theory and methods of machine learning and computer vision for different applications. He coordinated several research projects and co-authored more than 90 papers and 3 patents. He has also served as an associate editor for several special issues in remote sensing.



**Raphaël Canals** received the Dipl.Ing. degree in electrical engineering and the Ph.D. degree in electronics from the University of ClermontFerrand, France, in 1989 and 1993, respectively. In 1993, he was Postdoctoral Fellow at the Computer Science Department, CNRC, Ottawa, ON, Canada. In 1994, he joined the Polytechnic School, University of Orléans, France, as a Teacher. He is currently a Researcher with Laboratory PRISME, University of Orléans-INSA CVL. He is also an Associate Professor with the University of Orléans. In 2015, he was introduced at the AgreenTech Valley Cluster dedicated to digital technologies for plant industry. His current interests are in biomedical imaging, innovation for agriculture, the IoT, and AI.



**Rachid Nedjai** is a professor in limnology and geomatics at the University of Orléans, where he also leads the Master's program in Geographic Information Systems (GAED). He obtained his Ph.D. in geochemistry of lacustrine waters and paleoenvironmental reconstruction from the University of Grenoble 1. His research focuses on environmental data simulation, hydrogeology, and geomatics applications for water resource management. He has contributed to numerous international projects, including the redesign of Algeria's judicial map and a spatial data infrastructure for water management in Africa. He has supervised multiple theses on hydrology, water resource management, and environmental risk assessment, with many of his students successfully entering the professional world. His expertise in geomatics and water resource management has made him a key contributor to advancing sustainable practices in the field.